Final Scientific/Technical Report

DOE Award: DE-FE0012053

Project Title: Predictive LES Modeling and Validation of High-Pressure Turbulent Flames and Flashback in Hydrogen-enriched Gas Turbines

Submitted by

Noel Clemens (Principal Investigator)
Professor
Dept. of Aerospace Engineering and Engineering Mechanics
The University of Texas at Austin
512-471-4743
clemens@mail.utexas.edu

Venkat Raman (co-Principal Investigator)
Associate Professor
Department of Aerospace Engineering
University of Michigan
734-764-4318
ramanvr@umich.edu

DUNS Number: 170230239

Submitted to:

US DOE NETL
626 Cochran Mill Road
PO Box 10940
Pittsburgh, PA 15236-0940

Report Date: April 1, 2019

Reporting Period: 10/1/2013 - 9/30/2018

Disclaimer

Executive Summary

The overall objective of this project is to make advances in large-eddy simulation modeling of swirl-flame flashback at elevated pressure, where the reactants can be premixed or stratified, and composed of methane enriched with hydrogen. The modeling effort was conducted with a companion experimental validation effort that focused on high-speed measurements of flashback in a model swirl-flame combustor.

The modeling effort focused on the development of manifold-based combustion model for flashback simulations. The main complexity in this configuration comes from the flames' propagation through a stratified fuel-air mixture along with heat loss near the walls. For this purpose, a non-adiabatic flamelet model was developed and tested using canonical flow configurations. Further, extensive validation in premixed configurations is used to establish the model's accuracy in capturing heat loss and flame propagation. Finally, the model was tested using the UT flame flashback experiment, and was shown to accurately capture the flame flashback process. The end products from this work are a) a full validated flameout-based approach for modeling flame flashback; b) a complete implementation of the model in the open source OpenFOAM framework, which has been made available to both industry and academia; c) an extensive suite of validation studies performed using the OpenFOAM solver. In addition, new techniques for flame modeling, subfilter modeling of scalars, and simulation of low Mach number flows were developed and tested.

In the experimental validation effort, flashback was studied in a premixed and stratified swirl flame by using high-speed imaging diagnostics. Fuels tested included CH_4 enriched with H_2, with H_2 enrichment up to 84% by volume. These flashback experiments are conducted at pressures ranging from 1 to 5 atm. A swirler-based fuel-injection system was used to create the fuel-air stratification in the radial direction. For the high-pressure measurements, an optically accessible elevated pressure chamber was used. The spatial distribution of the equivalence ratio under non-reacting conditions was characterized using planar laser-induced fluorescence with acetone as the fuel tracer. It was observed that fuel-air pockets were distributed across the mixing tube width, although in an average sense, the fuel-air mixture was radially stratified. The global behavior of upstream flame propagation was investigated for different levels of hydrogen-enrichment. For stratified hydrogen-rich flashback, the propagation path of the flame changed from the inner wall to outer wall, which was induced by the faster chemistry of stoichiometric mixtures that are frequently present near the outer wall. This behavior of hydrogen-rich flashback persists even at elevated pressures up to 5 atm, although the propagation of the flame occurs as a wide flame tongue as opposed to the acute-tipped flame structures present in the atmospheric cases. The end product of the experimental effort is greatly improved knowledge of flashback physics and a unique database that can be used for model validation.

Table of Contents

A. Computational Program

1. Combustion models

This study was focused on flamelet-based tabulation methods for turbulent combustion modeling. The developments can be categorized into two groups: tabulations built with premixed flamelets and tabulations built with diffusion flamelets. These models were developed to capture the response of turbulent flame to physical effects that occurs in realistic gas turbines, e.g., heat loss, strain, and stratification. This section summarizes the results of model development in those aspects.

1.1 Premixed flamelet model

1.1.1 Non-adiabatic effects

Three non-adiabatic flamelet methods have been investigated: Method 1 solves a series of adiabatic freely propagating flame starting with different unburnt temperatures; Method 2 solves a series of burner stabilized flames with the same unburnt temperature but different massflow rates, which changes the rate of heat transfer at the inflow boundary, and eventually leads to different levels of total enthalpy; Method 3 is newly proposed and introduces heat loss via an artificial sink term in the flamelet energy equation. An example of the three methods is demonstrated in Fig. 1, by plotting the corresponding flame trajectories in physical space and phase space.

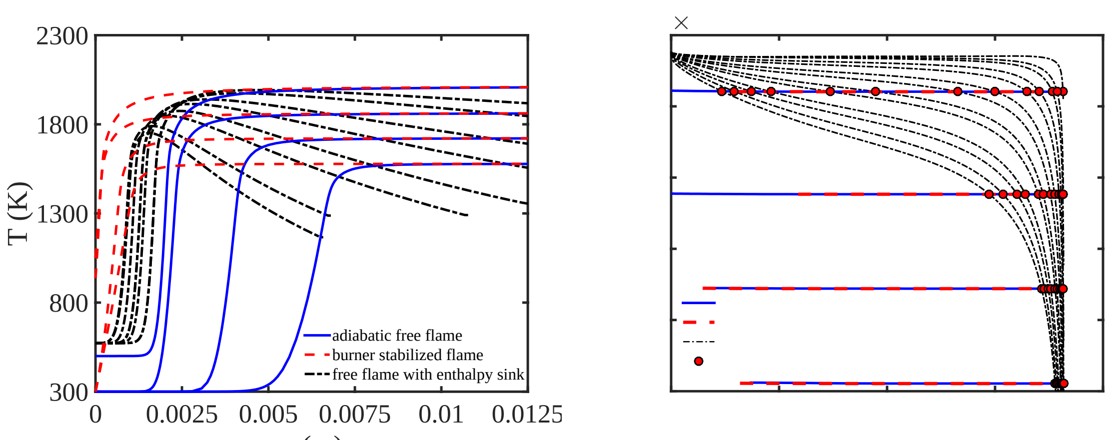

Figure 1. Three different modeling strategies for non-adiabatic premixed combustion. Left: physical space temperature profiles; right: trajectories in phase space of total enthalpy H_{tot} and progress variable defined as Y_{CO2}. The red dots mark the intersections of Method 3 with the Method 1 and 2, which is sampled for further comparison.

In this study, all three methods are realized and investigated. Here, the sink term in method 3 applies a novel development, which is formulated by Fourier's heat transfer law, as

$$S_d = -\lambda \frac{T(x) - T_w}{d^2},$$

where $T(x)$ is the local temperature of the 1-D flame, λ is the local heat conductivity, T_w is a presumed wall temperature that represents the interested configuration, and d is a parameter that has the same unit of physical length, which is used as the controlling parameter to achieve different magnitudes of heat sink. The modeling assumption of this strategy is by assuming the 1-D flame is transferring heat through a fictional wall with a temperature gradient of $(T\text{-}T_w)/d$. This is believed to be a canonical configuration that captures the effects of heat loss on the flame that has a flame-surface normal parallel to the wall. Method 3 was expected to predict the impact of heat loss differently than Methods 1 and 2, as it includes the change of total enthalpy along the 1-dimensional flame structure, which captures the interaction between heat release and the wall heat conduction. Whereas for Method 1 and 2, the enthalpy is simply maintained at a constant level for each individual flamelet (see r.h.s. plot of Fig. 1). However, a further comparison turned out to disprove this expectation, which is presented in the following paragraph.

Since Method 1 and 2 conserves total enthalpy, the resulting flamlet solutions can be directly compared to each other at the same enthalpy level. For Method 3, the enthalpy is not conserved within each flamelet solution, and those results need to be sampled at the phase space locations where its trajectories intersection with those of Method 1 and 2. The resulting sampling points has been highlighted in the r.h.s. plot of Fig. 1. Comparisons are made for both temperature and intermediate species, as shown in Fig. 2. It can be seen that the three methods closely match each other for both temperature and OH mass fraction, which means that while the flamelet methods may apply different assumptions on heat loss, the resulting flamelet solutions will end up being similar in the tabulation phase space. As a result, either of the three methods are equally applicable to construct a tabulation for non-adiabatic premixed combustion. In this study, the strain-free, non-adiabatic premixed tabulation was constructed using Method 3.

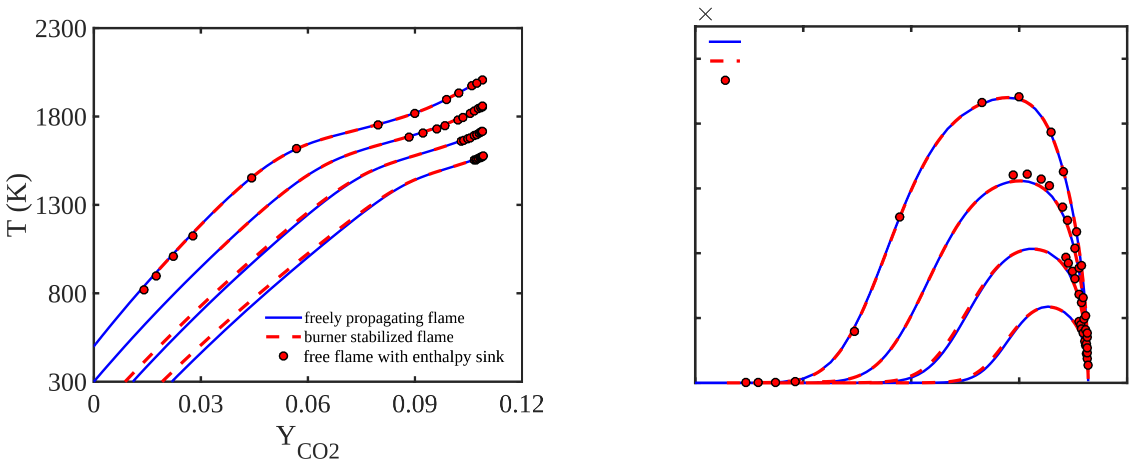

Figure 2. Comparison flames for the three methods. Left: temperature vs. progress variable at multiple enthalpy levels. Right: OH mass fraction vs. progress variable at multiple enthalpy levels.

The performance of the strain-free non-adiabatic flamelet was tested using a DLR 1-jet FLOX (flameless oxidation) combustor, which is characterized by a prominent recirculation zone and subject to large wall heat loss, as shown in Fig. 3. The results are compared against experimental measurements in Fig. 4, which shows improved accuracy compared to adiabatic flamelet results.

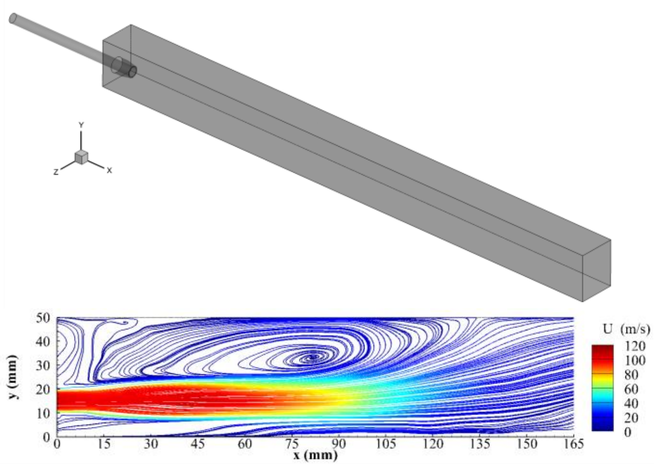

Figure 3. Top: configuration of DLR 1-jet FLOX combustor. Bottom: side view of time-averaged streamlines, colored with axial velocity contours obtained from LES simulation.

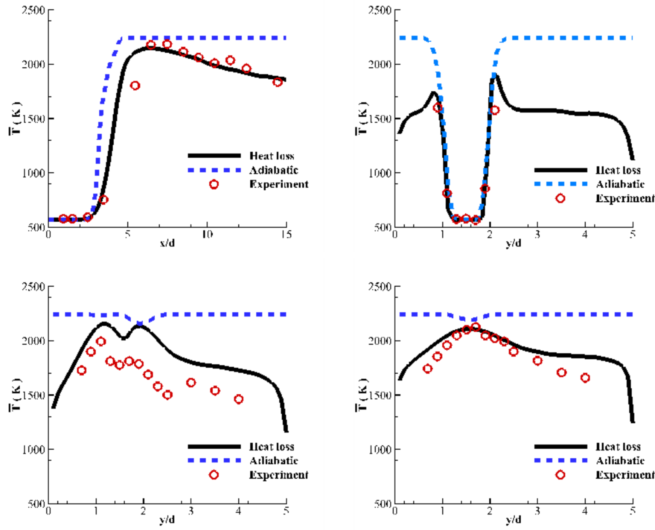

Figure 4. Temperature profiles obtaind from LES simulations using adiabatic flamelet model, non-adiabatic flamelet model and experimental measurements. Upper left: stream wise line at the jet center; upper right: vertical line at *x*=1*d*; Lower left: vertical line at *x*=5*d*; lower right: vertical line at *x*=8*d.*

1.1.2 Strain effects

Strain effects can be included into premixed flamelets using the configuration of a counterflow flame. The idea is similar to diffusion flamelets but where the two counterflowing streams are reactant and burnt product, instead of fuel and oxidizer. The amount of strain can be controlled by the inflow velocity. Results of the premixed counterflow flamelet calculations have shown that the flame peak temperature can decrease drastically with the increase of strain (Fig. 5, left), suggesting that strain effects could be an important factor affecting the premixed combustion systems. An extra advantage of the counterflow premixed flamelet configuration is that heat loss effects can also be included, simply by decreasing the burnt product temperature (Fig. 5, right).

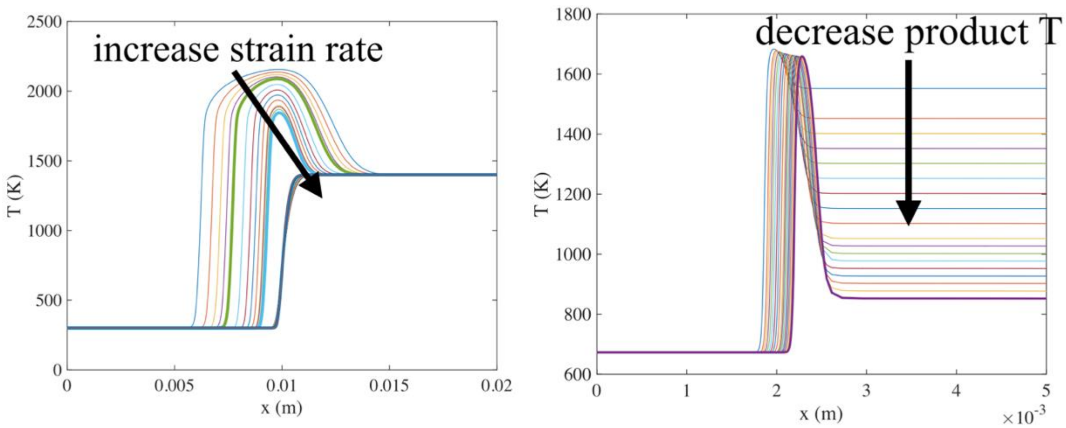

Figure 5. Temperature profile of counterflow premixed flamelets obtained with different strain rates (left) and burnt product temperatures (right).

A tabulation is constructed using these premixed counterflow flamelets; the methodology is demonstrated in Fig. 6. The local strain rate normal to the flame front is applied as an extra controlling parameter in addition to total enthalpy H_{tot} and progress variable C. During table lookup, this value can be obtained from the LES simulation. The performance of this combustion model is further tested using the above introduced DLR 1-jet FLOX combustor, with results shown in Fig. 7. It can be seen from the results that the strained non-adiabatic model predicts the temperature field that matches better with the experimental measurements than the non-adiabatic model.

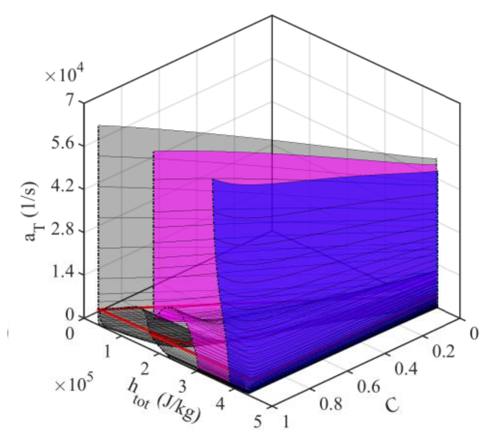

Figure 6. Demonstration of the construction of the strained, non-adiabatic premixed flamelet tabulation. Each trajectory corresponds to a flamelet solution, and each surface is a family of counterflow premixed flamelet solutions obtained under a fixed burnt temperature but various mass flow rates.

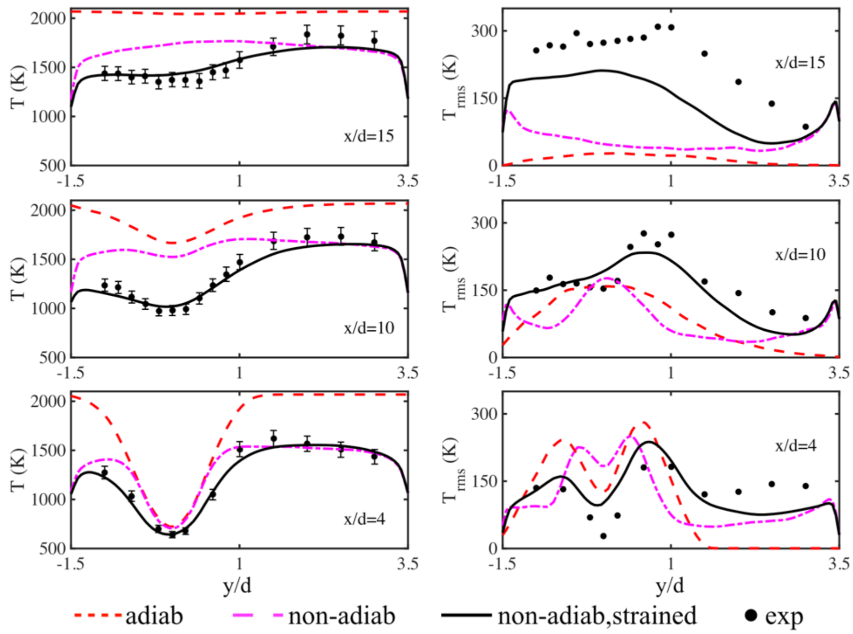

Figure 7. Temperature mean (left) and root mean square (right) profiles in vertical direction at different downstream locations of the DLR 1-jet FLOX combustor.

1.2 Diffusion flamelet model

1.2.1 Non-adiabatic effects

For diffusion flamelet models, the typical application is in non-premixed combustion systems. Non-premixed combustion systems like aircraft combustors usually do not apply any preheating of reactants. In this regard, the implementation of Method 1 to model heat loss is no longer straightforward. This is because the adiabatic unburnt condition here is already at a low ambient level (~300 K), such that a further decrease of this value as in Method 1 can easily lead to non-physical results in a thermodynamic sense. Method 2 is also not straight-forward to apply, as it requires extra effort to adapt the inflows of the diffusion flamelet to be burner-stabilized. At this point, Method 3 provides the most implementation-friendly option, as it simply requires the inclusion of a sink term into the flamelet energy equation. An example of the non-adiabatic diffusion flamelet model built by Method 3 is shown in Fig. 8.

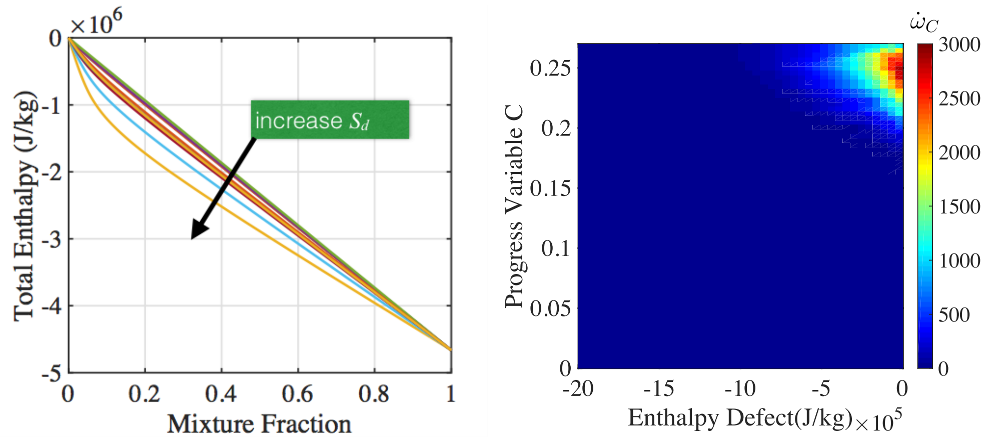

Figure 8. Demonstration of the construction of non-adiabatic diffusion flamelet model. Left: Phase space trajectories of populated flamelets; right: contour of reaction source of the resulting tabulation.

1.2.2 Strain effects

The effect of strain has already been included and translated into scalar dissipation rate in diffusion flamelets. In steady flamelet tabulation, the scalar dissipation rate is directly applied as the controlling parameter of the tabulation; in flamelet progress variable tabulation, the strain effect is mapped onto a progress variable. These methods have been previously studied in detail. However, combined with the effects of heat loss/gain, the strain rate response of diffusion flamelets may behave differently from that of conventional diffusion flamelets. For instance, under certain level of heat loss, the locus $T_{\max}$ vs. χ_{st} can transit from the conventional S-shape curve into a O-shape loop (l.h.s. plot of Fig. 9). Besides, when enthalpy is elevated from the inflow temperature, the turning point of the S-shape curve can disappear (r.h.s. plot of Fig. 9). This is referred to as partial extinction, and is due to reaction becomes more resistant to strain at higher inflow temperatures.

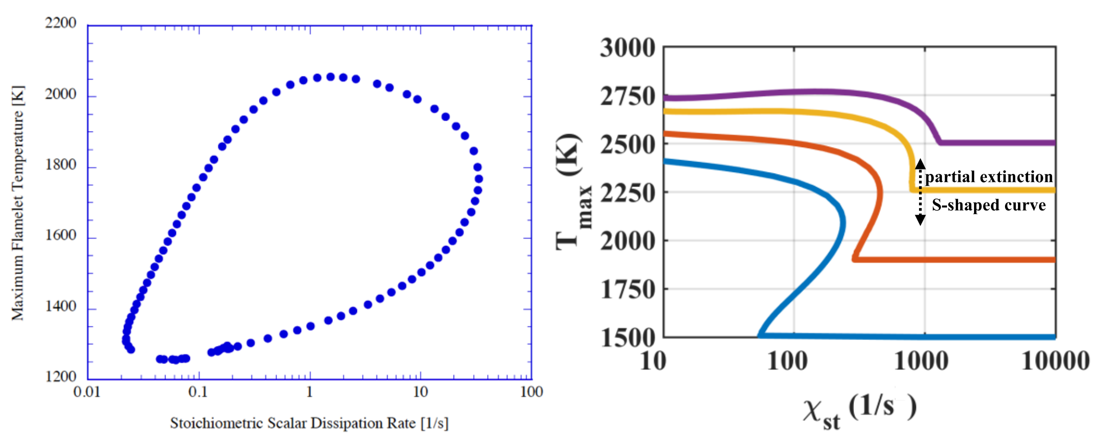

Figure 9. Locus of maximum temperature vs. stoichiometric scalar dissipation rate under large heat loss (left) and high enthalpy (right). The l.h.s. plot is obtained from Pitsch, 2006.

These above effects of enthalpy change may lead to extra modeling challenges. E.g., the FPVA tabulation may no longer be straight forward for an O-shaped loop, as the mapping of flamelet solutions with different $T_{\max}$ onto a progress variable is no longer single-valued. The modeling strategies for these situations may deserve more investigations in future study.

1.3 Mixed regime combustion - premixed vs. diffusion flamelet

The abovementioned premixed/diffusion flamelet models are unambiguously applicable for premixed or non-premixed combustion system. However, in certain situations such as in flame flashback in heavy-duty gas turbines, the flame front can propagate from the fuel well-mixed combustion chamber towards the upstream fuel-mixing section, where the reaction mode falls into a mixed regime between premixed and diffusion flame. Simply from a technical aspect, both premixed and diffusion flamelets can be applied to construct tabulation models of mixed-regime combustion. For diffusion flamelets, the implementation is the same as an FPVA method; for premixed flamelets, the flamelets need to be populated for a range of equivalence ratios to represent the stratification of fuel, as demonstrated in Fig. 10. However, whether premixed or diffusion flamelets are suitable as the canonical solution to model a mixed-regime combustion remains an open question.

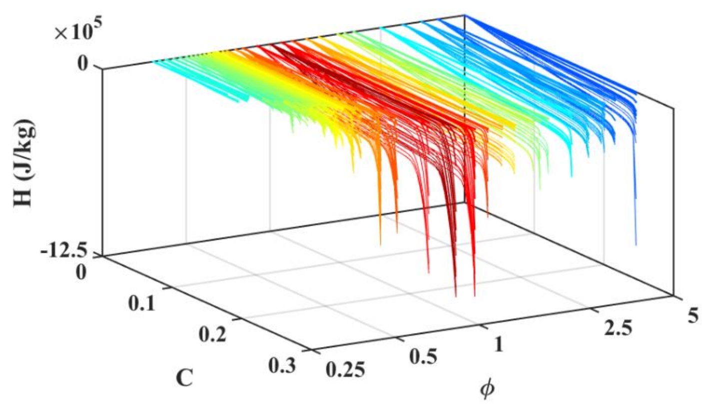

Figure 10. Trajectories of premixed flame flamelets applied into the tabulation of non-adiabatic stratified combustion.

Previous and on-going attempts to model mixed-regime combustion includes applying blended modeling strategies, or classification techniques that decides the switch between the two models during simulation run time. Here, instead of including extra treatments, both two models are simply tested and directly compared against each other. The goal is to find the trend of performance between the two models. For that, a priori study is first carried out to compare the two flamelets. The two flamelets are compared at the intersections of their phase space trajectories, as shown in Fig. 11.

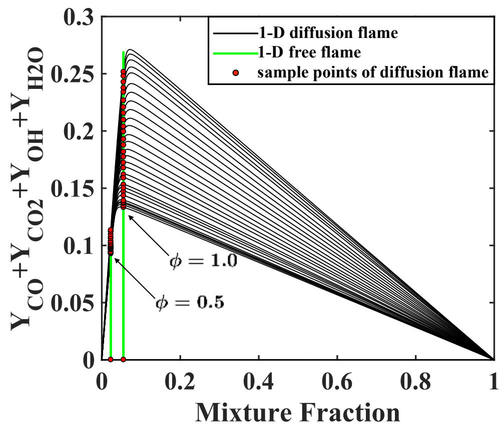

Figure 11 Phase space trajectories of diffusion and premixed flamelets. Diffusion flamelets are sampled at red points to comparison against the premixed flamelet.

Two equivalence ratios are chosen for comparison, and interestingly the two configurations show different relations based on the equivalence ratio. See Fig. 12, at equivalence ratio of 0.5, the diffusion flame has a source term peak value almost twice as large as the premixed flame. Whereas at equivalence ratio of 1.0, the free flame has the larger chemical source than the diffusion flame. This suggests that for well-premixed combustion, modeling by diffusion flamelets tends to under-predict reaction near stoichiometric conditions, while it over-predicts reaction at a leaner condition, and vice versa for non-premixed combustion.

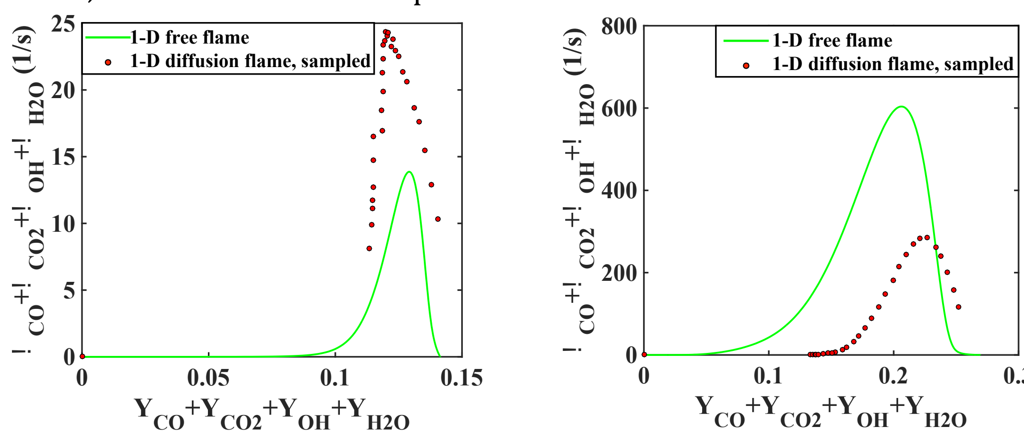

Figure 12 Comparison of chemical source obtained with diffusion flame and freely propagating flame. Results plotted in progress variable space with two equivalence ratios. Left: equivalence ratio = 0.5. Right: equivalence ratio = 1.0.

A flashback study of the UT High Swirl Combustor is presented in the following section. Both models are tested and compared with experimental results. The dominating mode of reaction is discussed below.

2. Flashback simulations

The configuration of the UT High Swirl Combustor is presented in Fig. 13. Pure fuel is injected through the ports located on the swirler surfaces. Fuel-mixing takes place downstream within the mixing tube. The fuel/air mixture becomes well-mixed further downstream within the combustion tube where the flame is originally stabilized. To trigger the flashback, a step increase of the fuel mass flow rate is applied. The flame front will then propagate upstream and enter the mixing tube, which is a mixed-regime combustion between premixed and diffusion flame. The flashback mechanism here is featured by a boundary layer type flashback while combined with a swirl motion.

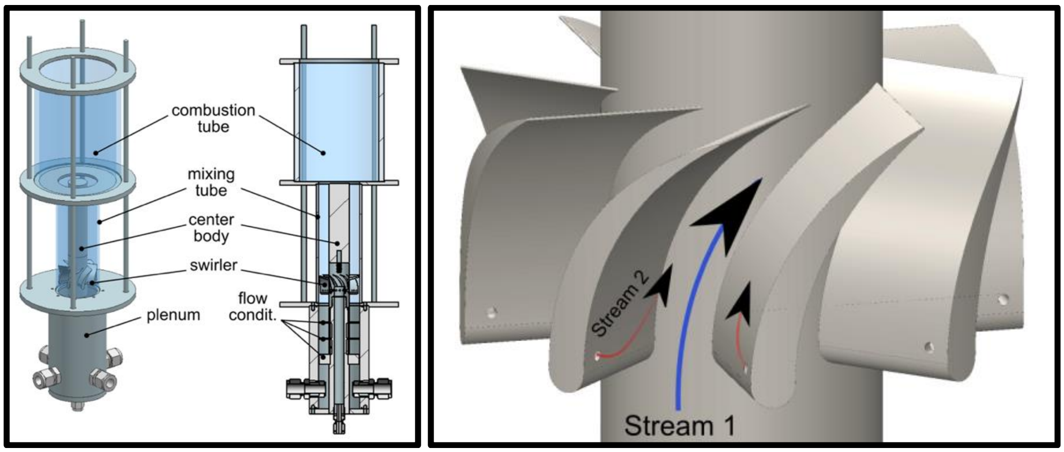

Figure 13. Schematic of the UT High Swirl Combustion (left) and a local zoom in near the swirler with fuel injection port (right).

2.1 Coldflow simulation of fuel mixing

The statistical distribution of the equivalence ratio is measured within a sampling plane (27 mm ×13.5 mm) located 42 mm upstream of the mixing tube exit. Within this sampling domain, two subdomains of different ranges of radial locations are further defined, as r < 6 mm and r > 6 mm. Both numerical and experimental results are shown in Fig. 14. It can be seen that the spatial distribution of the equivalence ratio match experimental results in terms of the range and the peak location of the probability density function of the equivalence ratio inside the sampling plane. It can also be seen that the fuel distribution is richer at the outer radius location of the mixing tube, which is mainly due to the location of the fuel injection ports being closer to the outer wall.

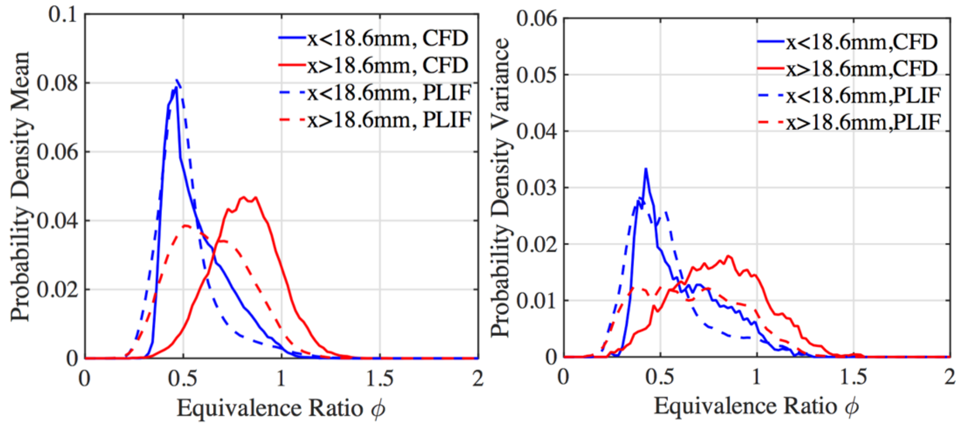

Figure 14. Time average equivalence ratio distribution obtained from numerical simulation and experiments (left). Root mean square equivalence ratio distribution obtained from numerical simulation and experiments (right).

Besides the statically steady flow field, the response of fuel mixing to the increment of fuel injection is also studied. The above developed flow field ($\phi = 0.5$) is applied as the initial flow field. At t = 0 ms, a step increase of fuel injection targeting $\phi = 0.63$ is enforced. The resulting evolution of the mixture fraction field is shown in Fig. 15. The fuel concentration within the mixing tube responds to the step increase within 40ms, while it takes a longer time (>120ms) for the inner recirculation zone to see the change of fuel injection.

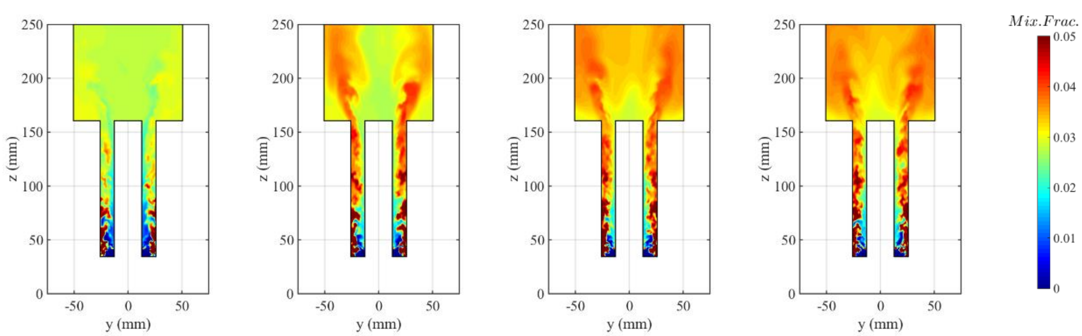

Figure 15. Time sequence of mixture fraction contours after an increase of fuel injection.

2.2 Reacting flow simulations

A series of flashback simulations were conducted, as listed in Table 1. The operating conditions here were not designed in advance, but in real time based on the result of the last simulation. The trace of this iterative process is summarized in two groups, as: P1->P2->P3; D1->D2->D3->D4. The process was driven by the following two considerations: For each model tested, if flashback was not achieved under the initial test conditions, i.e., equivalence ratio increased from 0.5 to 0.63 and adiabatic wall temperature, then increase the target equivalence ratio until obvious flashback is reproduced, which during practice led to P1->P3; otherwise, if flashback was achieved under the initial test conditions, then introduce more heat loss until flashback can no longer be produced, which during practice led to D1->D4.

Table 1. Operating conditions and results of flashback of all simulation cases and the experiment study. The 'Adiabatic' case here has a wall temperature of about 1800K.

Case ID	Model	Step increase of ϕ	Wall temp.	Flashback
P1	Premixed	From 0.5 to 0.63	Adiabatic	no
P2	Premixed	From 0.5 to 0.70	Adiabatic	dubious
P3	Premixed	From 0.5 to 0.75	Adiabatic	yes
D1	Diffusion	From 0.5 to 0.63	Adiabatic	yes
D2	Diffusion	From 0.5 to 0.63	1250K	yes
D3	Diffusion	From 0.5 to 0.63	1000K	dubious
D4	Diffusion	From 0.5 to 0.63	300K	no
Experiment	N.A.	From 0.5 to 0.63	Non-adiabatic	yes

The time sequence of progress variable contour of the cases of P1-3 are further plotted in Fig. 16. In P1, the flame is always anchored at the exit of the mixing tube, with its 'root' moving only slightly upstream after the richer fuel inflow eventually entered the inner recirculation zone (after 120ms). Notice that the operating conditions of P1 should be comparable to the experiment study. The premixed flamelet model failed to reproduce the occurrence of flashback.

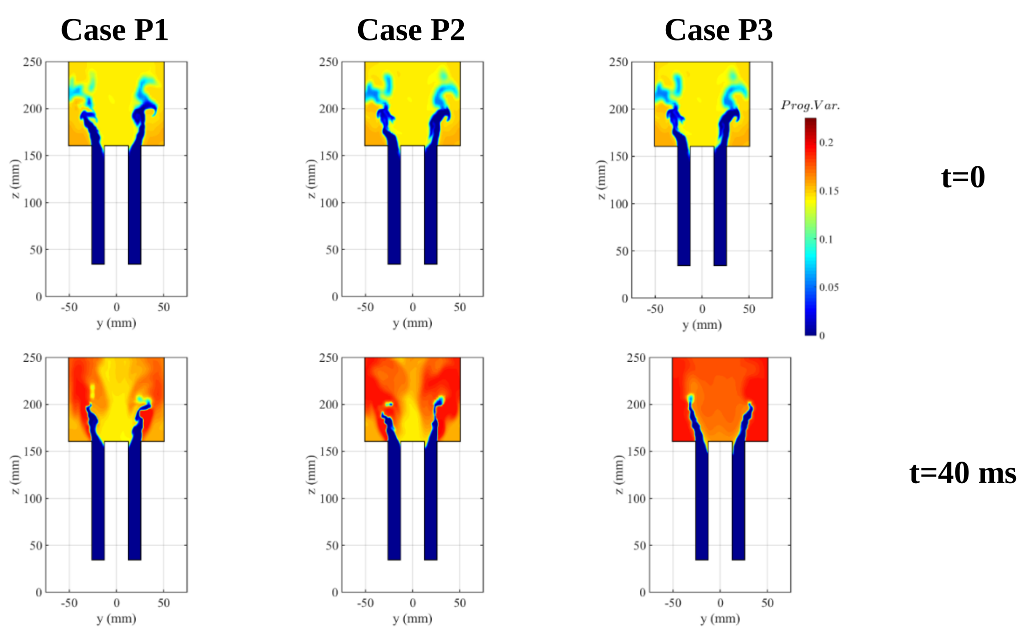

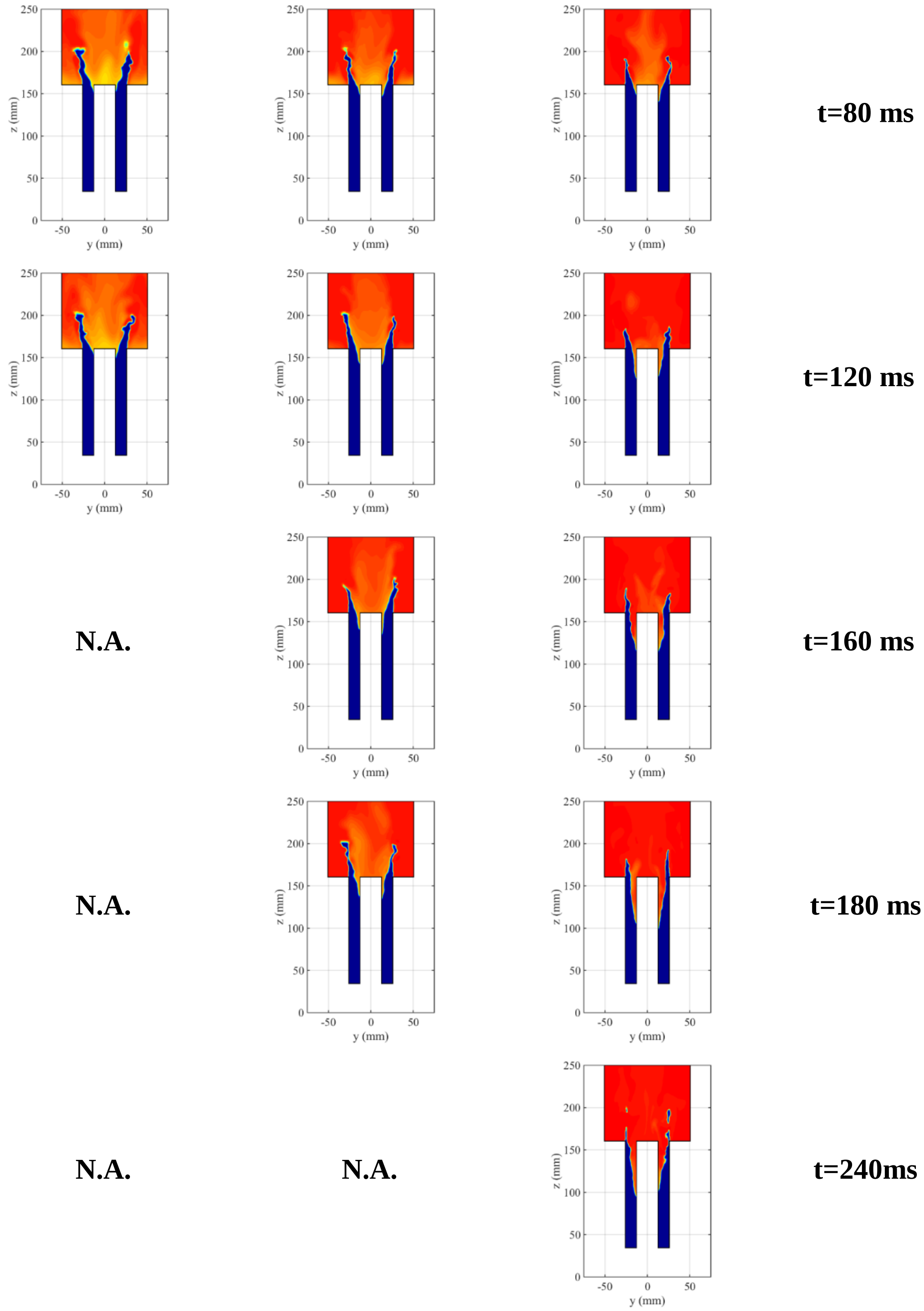

Figure 16. Time sequence of progress variable contour of P1-P3. Data are not available for some time instances as the simulations are terminated as soon as flashback was arrested.

To reproduce flashback with the premixed flamelet model, higher equivalence ratios were tested, i.e. case P2 and P3. The results are also presented in Fig. 16 to offer a side-by-side comparison with P1. It can be seen that at a target global equivalence ratio of 0.7, the flame front did enter the mixing tube, while only for a rather short distance before it was arrested. It was not until the target equivalence ratio value was set to 0.75 that a strong flashback was eventually observed.

In comparison, the simulations with diffusion flamelets were able to successfully reproduce flashback until the wall temperature was dropped below 1000 K (D1-D3). This is consistent with the priori study in the last section that diffusion flamelets tend to have higher reaction rates than premixed flamelet under lean conditions. These results suggest that the reaction mode in the mixing tube may be closer to a diffusion flame than a premixed flame.

3. Summary of the Computational Effort

- Combustion model developments
    - Non-adiabatic premixed flamelet model
    - Strained, non-adiabatic premixed flamelet model
    - Non-adiabatic diffusion flamelet (FPVA) model
    - Non-adiabatic premixed flamelet (FGM) model

- Flashback simulations
    - Fuel mixing captured with satisfying accuracy
    - Flashback captured with diffusion flamelet model

B. Experimental Program

4. Experimental set up

The flashback experiments were conducted with an annular swirl combustor which was mounted inside an elevated pressure chamber. A set of high-speed cameras and lasers were used to observe the flame propagation. In this section, we describe these experimental set ups in detail.

4.1 Swirl Combustor

The swirl combustor assembly used in these experiments is a lab-scale prototype of industrial combustors as shown in Fig. 17.

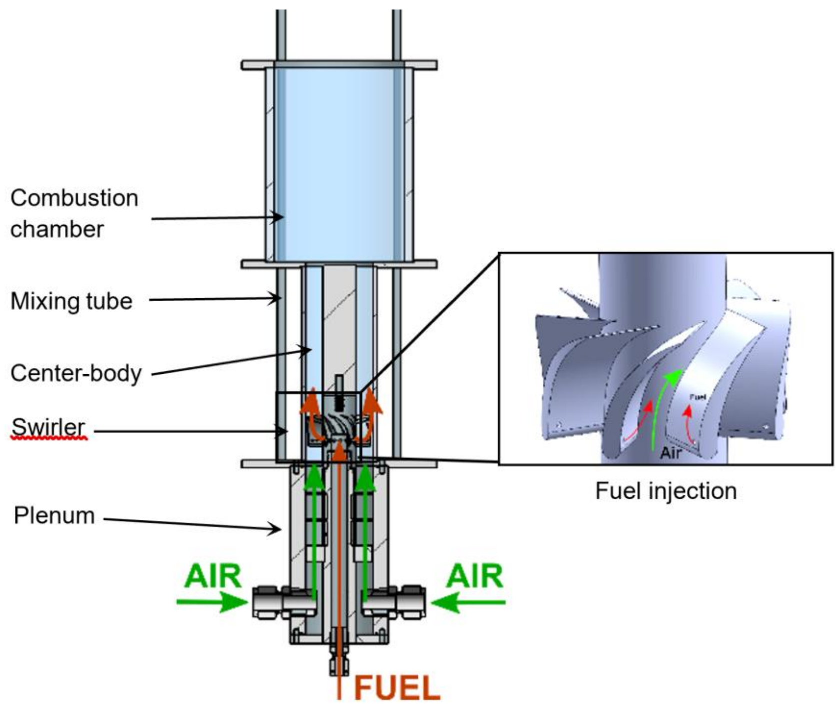

Figure 17. The optically accessible swirl combustor. Swirl vanes and the fuel path is illustrated in the inset.

The swirl combustor can be divided into three main sections: the plenum, the mixing tube, and the combustion chamber. The main air flow through the combustor enters the annular plenum region through four inlet ports, positioned symmetrically around combustor center-line. Entry of air through these ports is depicted in Fig. 17. Afterwards, this flow gets conditioned by passing through annular honeycomb straighteners and two stations of fine-wire mesh. The flow then passes through the swirl vane and into the mixing tube. The mixing tube consists of a center-body and an outer cylindrical wall. The axial swirler is a prototype of an industrial swirler with an inner and outer diameter of 25.4 and 50.8 mm respectively.

The swirler body is made with cobalt-chrome and was three-dimensionally printed with an uncertainty of +/- 60 microns. It was equipped with eight symmetric aerodynamically-curved vanes. Each swirler vane was angled at 60 degrees with respect to the combustor axis. These vanes were also equipped with fuel injection ports for use in partially-premixed flashback experiments. The fuel-entry paths through these ports are different than the main air flow and shall be discussed in a subsequent paragraph. The axial swirler imparts large azimuthal momentum to the approach flow. Numerical simulations of the flow at the exit of the mixing tube indicated that the swirl number is 0.9. The swirl number is the ratio of azimuthal to axial momentum flux of the swirling flow. The near-unity swirl number indicates that the flow in the mixing tube is of high swirl, according to conventional definitions (Swirl number > 0.6). The center-body of the mixing tube is attached coaxially to the downstream end of the axial swirler. The center-body is a lathe-machined stainless-steel cylinder with an outer diameter of 25.4 mm. Prior to installation, the near-polish-finished center-body surface was painted with an ultra-flat black spray paint (Krylon 5BIEP), which was desired to minimize the reflected light signal off the center-body. The outer wall of the mixing tube was made of optical grade fused silica (Heraeus Suprasil 310), which allowed optical accessibility into the flow field upstream of the combustion chamber. The inner diameter of the outer wall was 52 mm. The annular space of the mixing tube was bounded by the center-body and the inner wall of the fused silica tube. To ensure that the fused silica tube could be mounted co-axially with the center-body, a specially-designed alignment apparatus and screw-tightening methodology (see appendix) was used. Downstream of the annular mixing tube, the flow opened up into the combustion chamber that had nearly twice the outer diameter of the mixing tube. The center-body end plane was flush with the mixing tube exit plane. The inner diameter of the combustion chamber was 100 mm and its axial length was 150 mm. The combustion chamber and mixing tube were held fixed by sandwiching these components between the holding plate at the top and the plenum plate, as shown in the Fig. 17. The glass-metal components were sealed by using 1/8" thick ceramic paper gaskets (custom cut, in-house), which could withstand temperatures in up to 1200 deg C. Additionally, the padding provided by these gaskets compensated for the thermal expansion mismatch between the steel and the glass.

The fuel streams through the swirl-vane injection ports follow a different flow-path prior to entering the mixing tube. The central space in the plenum was occupied by a hollow tube that was connected to the swirler and the center-body. The hollow tube was connected to a fuel line, independent of the main swirl flow lines. The inner regions of the swirler and the center-body were also designed to be hollow, thereby providing continuous access to the swirler vanes and the center-body. This access to the center-body was used to route thermocouples, which were used to measure the temperature of the centerbody during flashback.

Fuel was passed through internal passages in the swirl vanes and then injected into the main flow as shown in Fig. 18. The passages were cylindrical in shape and 3 mm in diameter. The fuel injection ports in the swirl vanes were 1 mm in diameter. Two ports were used on each vane. These fuel ports injected the fuel normal to the swirl vane surface, akin to a JICF (jets-in-crossflow) configuration. These ports were located at a radial position 3 mm away from the outer wall to introduce mean radial stratification in the mixing tube. It should be noted that this inner-fuel-flow-design is optimized by doing several iterations of 3D printed plastic swirlers. Thin-channel designs are prone to asymmetricity due to large relative machining error (6-10%) and the possibility of partial choking of flow paths due to contaminants in the flow line. To minimize such problems, all of the flow paths were kept straight (easy-to-clean) and orthogonal at branching nodes (easy to ensure symmetricity). As a qualitative way to ensure symmetric behavior across all flow passages, a laminar diffusion-flame test was developed.

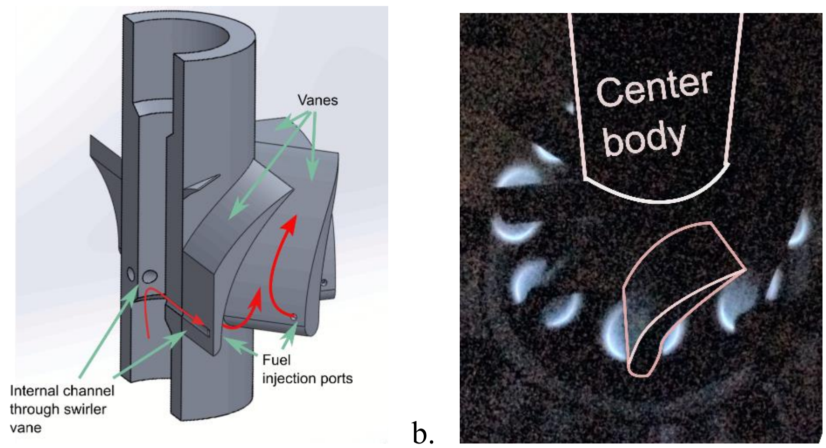

a. b.

Figure 18. (a) Cut out view of swirler showing the fuel path in red arrows, (b) Perspective view of the swirler during the laminar flame test. One swirler vane and the centerbody is highlighted.

In this laminar-flame test procedure, a very small amount of fuel was continuously flowed through the swirler vanes. Thereafter, diffusion flames were ignited in a fashion like a kitchen-stove burner. The resulting flame pattern, shown in Fig. 18(b), indicated the symmetric nature (or the lack of it) of the flow through the injection ports. Any loss of symmetry indicated a possible flow blockage problem, which was addressed by cleaning the fuel-ports. By repeating this procedure a few times, a reasonably symmetric appearance of the flames could be achieved. It should be noted that ensuring the symmetry of the flow is important to comment on the nature of flashback in partially-premixed flames.

Fuel flow to the combustor was supplied by industrial pressurized gas cylinders (Praxair or Airgas, 2500 psig when full, 99% purity) equipped with pressure regulators. The main air flow was supplied by a large pressure tank (maximum pressure: 150 psig) that was charged with air from the house compressor. These gas sources were connected to high-precision mass flow controllers (Alicat MCR series), which were given control input through an in-house written LabVIEW program (custom-edited Alicat software). The mass flow controllers had an accuracy of 0.1% of the full flow scale value. The gas-specific PID (proportional, integral, and differential) parameters of the mass-flow control were obtained by trial runs. These parameters were optimized to obtain a small response time, without overshooting the flow rates. Any overshoot beyond the fuel-flow set point may lead to undesired flame presence in the plenum or strong pressure fluctuations in the combustion chamber. A solenoid-driven shutoff valve was utilized to cut off the fuel-flow in such situations. Also, the flow control software was modified to ensure a quick and simultaneous control of multiple flow lines to avoid any untoward incident.

4.2 Elevated pressure chamber

An important purpose of this research is to understand how flashback occurs in an industrial gas turbine. Thus, to simulate the turbine conditions, a continuous-flow, backpressure-controlled elevated pressure chamber was designed and built. Although an actual gas turbine power plant reaches pressures up to 30-40 atm, the current chamber is designed to operate only up to 10 atm. Since the hot regions of the pressure chamber may reach high temperatures (up to 500 deg C), the pressure chamber was made of stainless steel, which exhibits excellent yield strength even at elevated temperatures. The chamber is designed for thermal heating powers up to 300 kW.

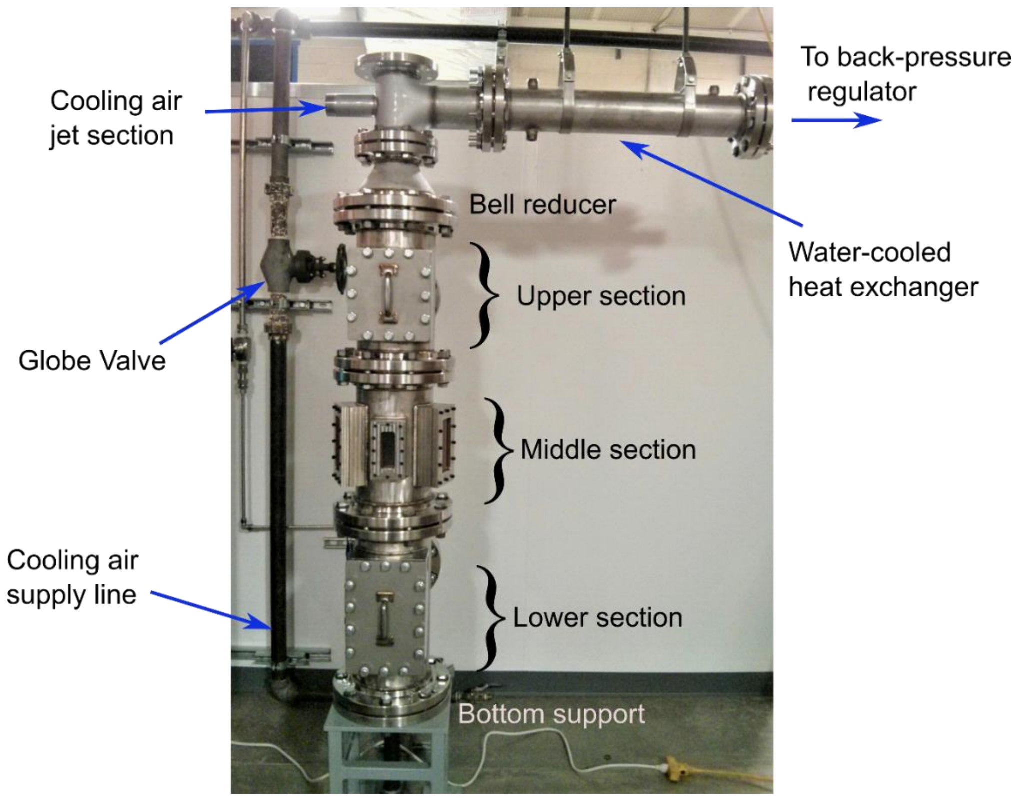

Figure 19. Photograph of the elevated pressure chamber.

The pressure chamber is shown in Fig. 19. This chamber is provided with two rectangular access ports that allow for manual access to the internal assembly. Four different fused silica windows were incorporated into the pressure chamber such that high-pressure laser diagnostic experiments are carried out. The lower section provides the platform for the experimental set up installed inside the chamber. It has a blind-flanged connection on the side that offers a flat surface for fuel entry ports. It also has an access door on opposite side that is useful for the installation and adjustment of internal assembly. The inlet for the cooling air co-flow is provided at the center of the bottom face. The inlet of cool air co-flow is shown in the cut-out image of the pressure chamber in Fig. 20.

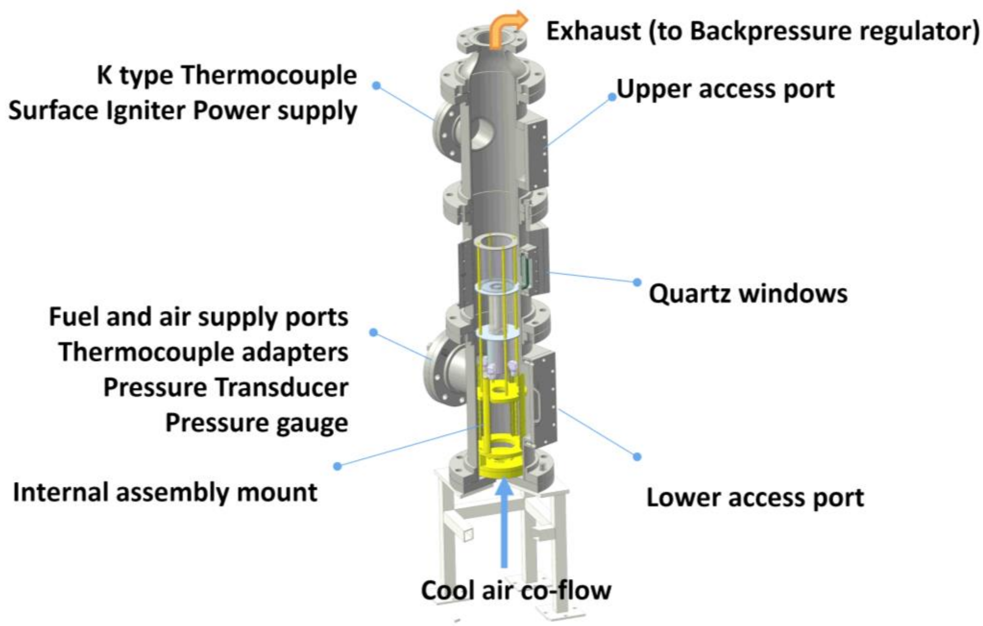

Figure 20. Section view of the pressure chamber showing the internal assembly

The middle section consists of three rectangular windows, two large ones (6" × 2.4") and a smaller one (4" ×1.5"), to allow optical access to the test section. The axes of the larger windows are at an angle of 70 deg with respect to the smaller window in the horizontal plane. The orientation of the large windows allows for stereoscopic PIV to be conducted. The windows are made of S1UV fused silica glass (Esco Optics), which have high transmission for UV light.

The upper section features another access gate, which was primarily used to install the calibration target for stereo PIV. Attached to the upper section is a bell reducer, which acts as a passage for the hot exhaust gases. The smooth transition from 8-inch diameter to 4-inch diameter piping allows for streamlined flow of the cooling air. This geometry maintains low acoustic noise in the chamber, which is necessary for safe operation. At the top of the chamber, another window is provided to allow for a laser sheet to enter the chamber. To shield this window from hot gases, additional cooling air is supplied from the side that reroutes the exhaust and decreases the sudden rise in temperature at the glass surface. A thin sacrificial glass plate is provided in the window assembly to protect the main window from the hot gases. The high pressure chamber is versatile in the sense that it can host various combustor geometries. Air mass flow rates to the combustor of up to 0.1 kg/sec are possible, which corresponds to a Reynolds number of 200,000 at 150 psi based on the tube diameter of 50 mm. The chamber is designed for thermal heating powers up to 300 kW. The vertical pipe assembly offers great adaptability for different visualization methods. Depending on optical access requirements, the middle section can be replaced to allow alternate window locations. The top window is ideal to observe the flashback process in a transverse plane.

Safety has been given utmost importance in designing of this pressure chamber. The glass windows have been designed with a high safety factor (~10). A pressure safety valve is provided in the bottom section of chamber. The cooling air supply tank is kept at the maximum of 150 psi which is also the maximum design pressure of the chamber. Thus, during operation, the pressure chamber is inherently safe against any unintended rise in airflow.

4.2.1 Flow through the pressure chamber

Figure 21 shows a simplified process and instrumentation diagram for the pressure chamber. The cooling air is supplied to the pressure chamber from a medium pressure gas tank (maximum pressure 150 psi) located at the Wind tunnel lab, Pickle Research Campus. The flow through the supply line is controlled using a control valve that is normally-closed and is provided a diaphragm actuator pressure of 40 psi. A set of ball valves are included in the air supply line to isolate different sections of the process flow during start up. Fuel is supplied to the set up through industrial gas cylinders equipped with standard gas pressure regulators. A bank of high-precision mass flow controllers (Alicat scientific, +/- 0.2% full scale accuracy) are used to supply the air and fuel flow through the combustor. The cooling air co-flow is regulated using the globe valve (typical opening of a quarter turn) and the control valve. The cooling air supply line (diameter 2 inch) opens at the bottom flange of the pressure chamber. The cooling air jet spreads out in the pressure chamber (inner diameter of 8 inches) and flows around the internal assembly of the combustor. Upon crossing the combustor's location, the cooling air shrouds the inner walls of the pressure chamber and gradually mixes with the combustion products of the swirling flame.

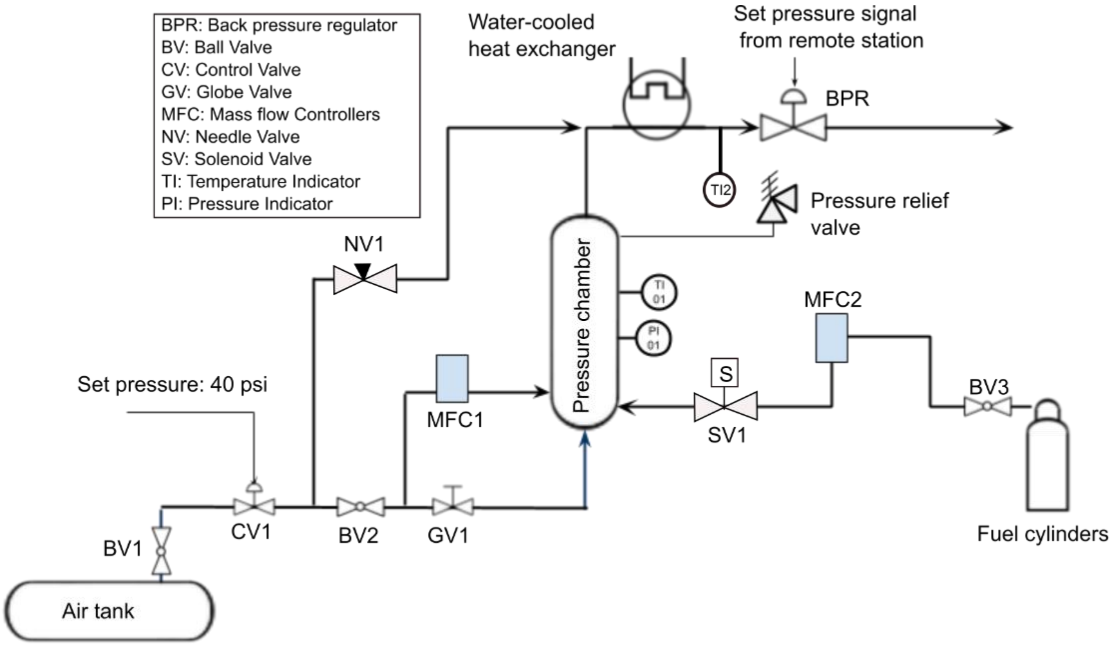

Figure 21. Simplified Process and instrumentation diagram for the pressure chamber.

The entire pressure chamber facility was operated remotely from a control station equipped with four different computer systems. These computer systems were remotely connected on the internal network to the master computers for processes such as image capturing and pressure chamber monitoring. In addition to the cameras for optical diagnostics, a set of security cameras were installed to monitor the experimental facility area during the experiments.

4.3 Optical diagnostics

4.3.1 Chemiluminescence imaging

High-speed chemi-luminescence imaging was used extensively to investigate flashback. For this purpose, a high-speed imaging camera (Photron APX) with a mounted external intensifier (HiCatt, Lambert Instruments) is used to capture the flame propagation. Depending on the experimental requirements, a 105mm Nikon lens (narrow view) or 70-250 Tokina lens (wider view) is used. Typically, luminosity images are captured at 4 kHz with an exposure of 250 microseconds. The intensifier gate is kept at 50 and 100 microseconds for methane-air and hydrogen-rich flames, respectively. For corresponding cases, the intensifier gain is kept at 750 and 850. During simultaneous laser diagnostics, a digital delay generator was used to sync the intensifier with the lasers such that the intensifier gate is closed during the laser pulse. In general, care was taken to avoid any reflection towards the intensifier. The center-body was painted black and any possible reflected light towards the intensifier was blocked. For further protection of the camera and the intensifier, the monitor current trip limit was set at 6%.

Interpretation of chemi-luminescence images depend on the global shape and propagation behavior of the flame that enters the mixing tube. If the flame surface topography remains consistent over length-scales and timescales of the observation, it can be assigned an identity. A simple example would be a spherical flame. Although the geometry of a flame tongue may or may not be geometrically consistent, the convex shape of the flame surface allows us to define a flame tip. The flame tip is the most upstream point of the flame tongue. When considering axial flame propagation, the axially-upstream point can be identified and defined easily. This point leads the upstream propagation of the flame surface and tracking it allows us to identify the axial motion of the flame tongue.

Luminosity signal is line-of-sight integrated in nature, which prohibits us from determining the three-dimensional position of the flame tip from a single projection of luminosity. However, previous studies in this facility of flashback for premixed reactants showed that the flame tip tends to stay close to the center-body as it flashes back. Thus, even with a single luminosity image, the location of the flame tip can be easily tracked.

Figure 22 shows the top view of the visible region in the mixing tube. The region behind the center-body is occluded for the luminosity imaging camera. The region on the left and right of the camera can distinguished on the basis of the angle subtended at the center. The left region extends from ($-2\pi/3 < \theta < 2\pi/3$), and thus any tracking of the flame structure could be done only in the non-occluded region. Given the line-of-sight integrated nature of luminosity signal, the depth of any flame feature detected in the left and right section would be difficult to comment upon.

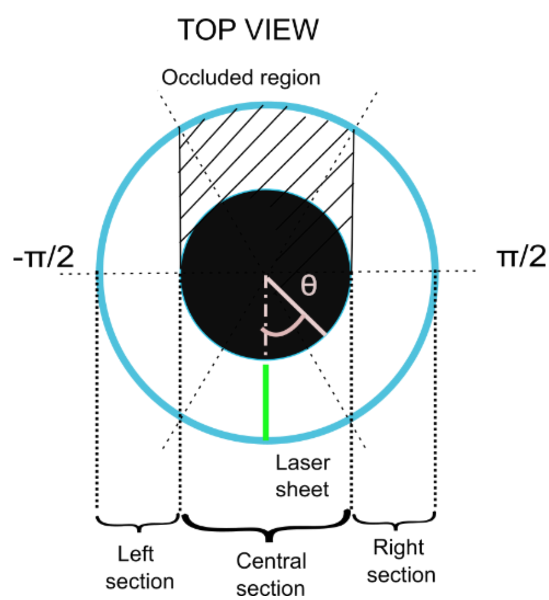

Figure 22. Top view of the mixing tube showing the region occluded for luminosity imaging. The position of the laser sheet and different regions of the field of view are shown.

4.3.2 Planar Laser Induced Fluorescence (PLIF)

Fuel-air mixing upstream of the combustor exit plane is quantified using acetone PLIF. Acetone has been widely used as a fuel-tracer, mainly due to its excellent fluorescence quantum yield, low toxicity and low cost. Acetone has an absorption spectrum which extends from 225 nm to 325 nm (ground level to first excited singlet transition). The fluorescence is emitted over the range of 350 nm to 650 nm. When excited with an ultraviolet beam the acetone fluorescence appears as blue-violet.

Acetone bubbler

To conduct the acetone PLIF experiments, the fuel flow is seeded with acetone vapor. Thus, to achieve this, the fuel line is passed through an acetone bubbler prior to entering the mixing tube. The bubbler is a cylindrical copper vessel filled with liquid acetone. The internal diameter of the bubbler is approximately 3.5 in. The copper vessel has a brazed brass top with a three-inch diameter female thread. This section is capped with a brass plug. To prevent continuous cooling of liquid acetone due to evaporation, water is passed through copper coils that are immersed in the liquid acetone. This system enables us to produce a high level of acetone enrichment without condensation in the fuel stream. The fuel flow enters the bubbler through a vertical half-inch tube that extends into the bottom of the bubbler. This tube is plugged at the end but is perforated to enable the gas to be injected into the liquid acetone like a shower head. As the gas rises it becomes more enriched with acetone vapor. The enrichment level depends on the residence time of the gas in the acetone bath, but typically saturated conditions could be achieved.

During flashback experiments, it was realized that the acetone tended to condense in the tube, which clogged the fuel tube over time. Thus, in order to prevent the excess acetone condensation in the tube, another cylindrical copper vessel was connected downstream of the bubbler. This vessel served as a condensate-accumulator and prevented liquid acetone build up in the fuel supply tube or the combustor.

Lasers and Imaging set up

In order to excite the acetone fluorescence, a sheet of 266 nm is passed into the mixing tube from the side, as depicted in Fig. 23. A scientific CCD camera (PCO 1400) is used to image the fluorescence from the acetone. This camera is placed normal to the laser sheet. Maximizing the fluorescence signal collection is important to get a good signal-to-noise ratio. Hence, the camera-mounted 50 mm Nikon lens is kept at its lowest f-number (f/1.2). A 12 mm extension tube is used to enable focusing of the camera lens for the short working distances used. The camera was turned by 90 degrees to help match the aspect ratio of the field of view. The pixels were binned 2x2 to improve the SNR (Signal to Noise ratio). To minimize the background noise, an ultra-flat black painted surface is kept in the background. For high-pressure PLIF measurement, the inner wall of the pressure chamber on the opposite side of the laser sheet is painted black.

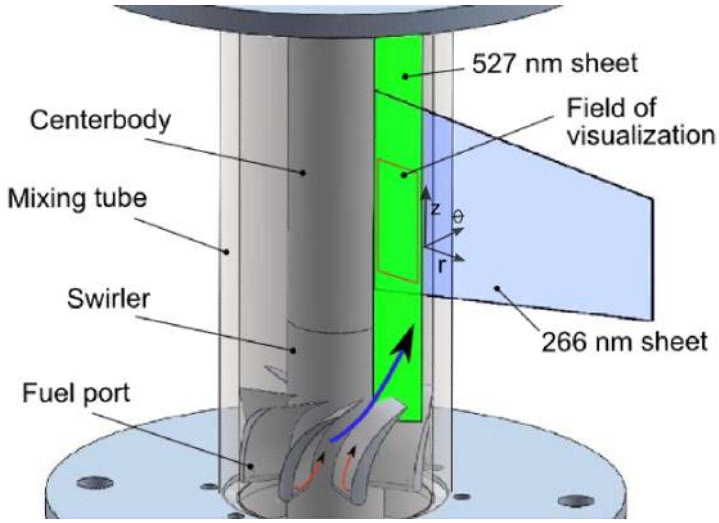

Figure 23. Schematic diagram of the field of view inside the mixing tube. A 266 nm sheet is brought from the side of the mixing tube.

A colored blue filter is placed in front of the camera lens to reduce any extraneous signal. The 266 nm laser sheet is formed using a 532 nm pulse from Nd YAG laser (Continuum Powerlite DLS 9010). The one-joule 532 nm pulse is passed through a frequency-quadrupling KD*P crystal (Spectra Physics). Frequency-quadrupling is a highly non-linear process whose efficiency is dependent on factors such as crystal temperature, incident angle of the beam on the crystal and polarization of the laser beam. Thus, prior to running the PLIF experiments, the frequency quadrupling is maximized by tuning the crystal inclination and temperature. The output beam from the crystal consists primarily of 532 nm and 266 nm beams. The residual green laser is filtered by passing the beam through three 255 nm dichroic mirrors. The frequency quadrupling is continuously tracked using a power meter (Coherent FieldMax II-TO), while tuning the crystal. Once tuned, the crystal is not disturbed until the experimental campaign is over. It was noted that the shot-to-shot variation could be as high as 50% during experiments, even though the crystal inclination and temperature settings was kept the same. This issue might be because of the local variation in the crystal temperature, although the exact reason could not be ascertained. Thus, to correct for this temporal variation in the pulse energy, the sheet energy and profile were measured on a shot-to-shot basis.

After the 266 nm beam is passed through the sheet forming optics, a fused silica flat is used to reflect a fraction of beam (~4%) towards a cuvette (CV10Q3500F-E, ThorLabs) filled with a mixture of fluorescent dye and water. The rest of the beam is directed towards the mixing tube. The cuboidal cuvette (10 mm x 10 mm x 50 mm) allows the beam to enter through its flat surface and is then absorbed by the fluid. The fluorescence is captured by another scientific-grade CCD camera (PCO Pixelfly). This camera is synced with the operation of PLIF imaging camera to enable simultaneous capture of the PLIF data and the fluorescence from the dye in the cuvette. The cuvette fluorescence provides a measure of the pulse-to-pulse variation in the laser energy and the sheet profile. The location of the cuvette and the field of view are positioned symmetrically with respect to the fused silica plate, which enabled the laser sheet profile to be of same dimensions as that of the PLIF imaging field. However, the optical path length of the beams are still not completely symmetric since the laser sheet passes through the mixing tube wall. Owing to its curvature, it can still cause some lensing effect on the beam, however since the laser sheet as well as the cylinder is vertical, it should have minimal effect on the vertical profile. In order to register the laser sheet profile correspondence between the cuvette image and the field of visualization and an optically opaque object such as an Allen key was placed in the path of the laser beam. Figure 24(a) shows an image of the mixing tube filled with acetone vapor. The blockage of the laser beam is visible in the image. Figure 24(b) shows the fluorescence from the cuvette, which also shows the shadowed region.

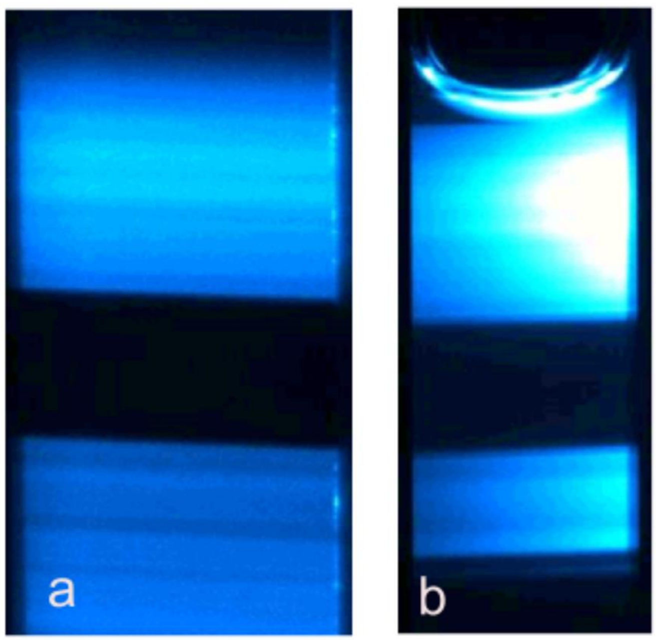

Figure 24. (a) PLIF signal from the laser sheet after partially blocking the beam, and (b) simultaneous laser sheet profile in the cuvette.

Using this method we could correct the laser sheet profile on a shot-to-shot basis. The sheet-profile apparatus also provided us with an improved means of controlling the 266 nm beam energy fluctuations. During experimental runs, the PLIF images were monitored using the live view mode of the PCO camera. Depending on the PLIF signal intensity, the crystal phase-matching angle was varied such that the frequency quadrupling was maximized. In this way, the SNR could be improved by as much as 200%. A typical variation in shot-to-shot pulse energy is plotted in Fig. 25.

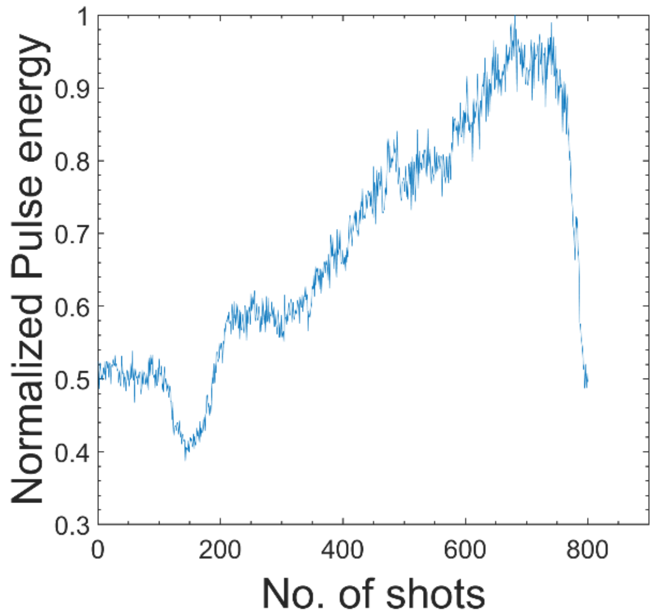

Figure 25. Typical shot-to-shot variation in 266 nm beam over time as measured from the cuvette signal.

Another issue with PLIF imaging in a confined flow arises from the scattering from the neighboring surfaces. In the atmospheric pressure set up, reflections could be minimized by tracking the source of the reflections and blocking them or judiciously painting components black. On the other hand, in the elevated pressure chamber, the process is more challenging. There are primarily two reasons for this. The first is that the laser sheet correction method could not take into account any possible change in the laser sheet profile due to dust at the flat windows. In particular, we observed that the laser sheet profile in the cuvette and the mixing tube were not the same. The second is that the scattering from the windows and the inner walls of the pressure chamber could induce additional background in the PLIF images, which could not be accounted for by the sheet correction. In order to reduce this background interference, the pressure chamber windows were almost entirely blocked except for a slit that allowed the laser sheet to enter the pressure chamber. A sample background-corrected PLIF image is shown in Fig. 26. The colorbar indicates the pixel value. The vertical straight lines in the region 6 mm $< r <$ 8 mm are due to the scattering that cannot be corrected even by shot-to-shot correction.

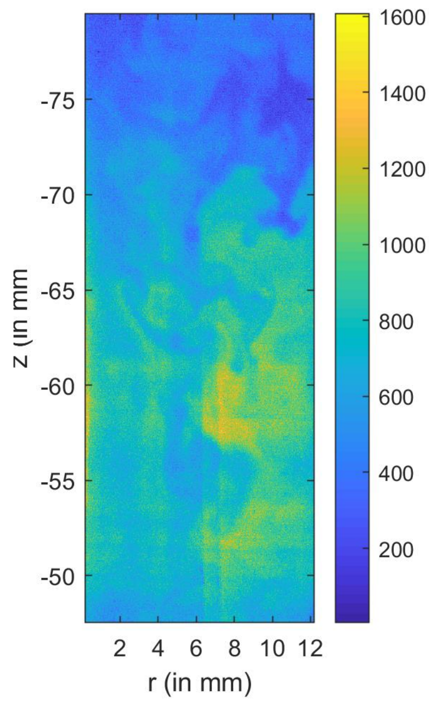

Figure 26. Background-corrected PLIF image for methane-air mixing at 3 atm, Re_h = 18600.

4.3.3 Fuel air ratio determination

The acetone fluorescence signal F(x,y) is directly proportional to the local laser fluence and concentration of acetone. In general, the acetone fluorescence depends on the local temperature, but in the current study this method is primarily used under isotheral conditions. The pixel intensity I(x,y) in a PLIF image is the sum of background, intrinsic camera noise and the fluorescence. The background noise is usually related to scattering from surfaces and windows, or fluorescence from unintended sources such as windows or paints. The intrinsic noise in the camera is mainly due to readout noise. To separate the fluorescence signal, the background signal is subtracted from the PLIF image. The background image B(x,y) is obtained by capturing the image without any acetone present in the flow field. The background signal is shot-dependent and any shot-to-shot variation in laser energy causes it to fluctuate. It is not an issue when the fluorescence is an order of magnitude higher than the background, however in fuel-air mixing for very lean patches, it can lead to significant error. Thus, accounting for shot-to-shot variation helps in reducing the background noise. The shot-adjusted background signal has been used in this study. Once this image is subtracted from the shot-adjusted PLIF images, the resulting signal is an outcome of the fluorescence from the acetone. To obtain 'pure-fuel' fluorescence, the mixing tube is filled with acetone-saturated air. The mixing tube is plugged with an annular Teflon plug and "pure-fuel" is added to the mixing tube. This pure-fuel signal P(x,y) is then corrected for the shot-to-shot variation in the laser pulse. The shot-adjusted background signal is then subtracted from the shot-adjusted pure-fuel signal. The resulting image provides the fluorescence from the maximum concentration of acetone. The fuel-air ratio at a point can be calculated by dividing the shot-adjusted background-corrected PLIF signal of fuel-air mixture with the corresponding pure-fuel pixel value. The final image provides the spatial distribution of fuel-air ratio in the mixing tube.

For these experiments, the SNR is found to be in the range of 24-30 in fuel-rich regions, while in fuel-lean regions the signal could be as low as the background. The fluorescence data is affected by the laser sheet absorption as it passes through the field of view. In addition, the scattering off the inner-wall of the mixing tube and hence the background signal may vary from shot-to-shot because of fluorescence itself. These factors are relatively low in magnitude (<10%) and difficult to correct for. Hence, the image processing does not account for these errors.

4.3.4 Particle Image Velocimetry

High speed stereoscopic PIV measurements were taken during the flashback runs. A pair of Nd:YLF lasers (Coherent Evolution 90) were used to get a pair of laser pulses which were combined and expanded into a laser sheet entering the swirl combustor from the top. This arrangement of laser sheet allowed the illumination of the boundary layer on the centerbody without much scattering off the wall. By bringing the laser sheet from the top, the forward scattering of laser sheet was captured by high speed cameras (Photron APX). These high-speed cameras were tilted with respect to the laser sheet. Hence, to keep the particles in focus, scheimpflug adapters were mounted on the camera. These adapters were adjusted to satisfy the scheimpflug criteria. This arrangement of the laser sheet and the cameras are illustrated in the schematic as shown in Fig. 27. A set of digital delay generators (SRS DG535) were used to sync the lasers such that there is a delay of 80 microseconds between laser pulses. At the same time, camera trigger and the frame rates were adjusted such that both cameras capture simultaneous particle images. These cameras were operated in "End" trigger mode which allowed the data to be captured with a manual trigger. Camera operations were controlled using Photron software (PFV 0.63).

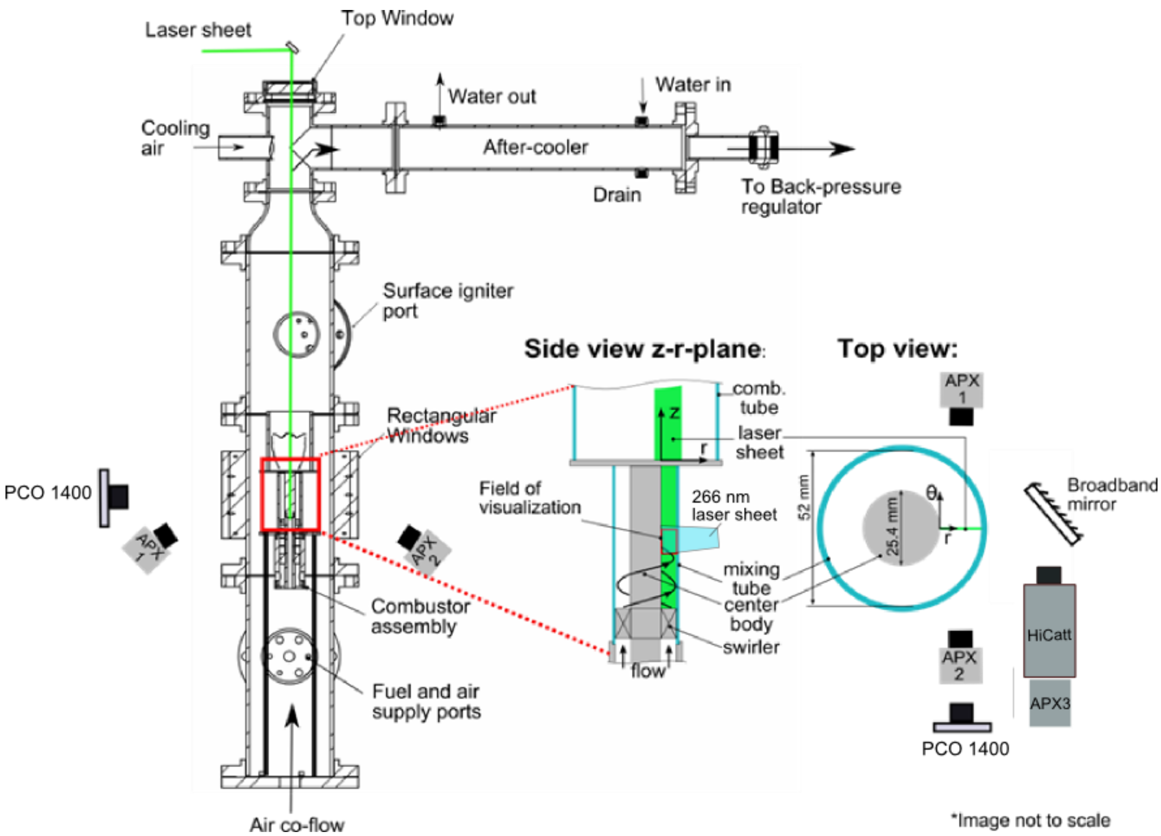

Figure 27. Optical diagnostic set up for elevated pressure experiments

Digital delay generator (SRS DG535) were used to provide a delay of 80 μs between laser pulses. The laser sheet thickness was kept at 1mm FWHM. The field of visualization extended from z = -80mm to z = -55mm where the z-coordinate is measured relative to the exit of the mixing tube. A calibration target of size 10 mm x 40 mm with dot spacing of 1 mm was translated normal to the measurement plane in the steps of 0.5 mm. Solid and liquid seeding particles were used to Mie-scatter the laser on to the particle imaging cameras. For liquid particle seeding, air flow is seeded with olive oil droplets of nominal diameter size of 1 micron. These olive particles are generated by flowing a fraction of air flow through the six-jet atomizer (TSI, Inc.). For solid particle seeding, titanium oxide particles with nominal diameter of 1 micron were used. For this purpose, a copper fluidized bed seeder was used to generate a uniformly seeded air flow. During experimental runs with solid seeding particles, the mixing tube inner wall would get covered with a fine layer of particles. So, after 2 to 3 runs, the combustor was disassembled to clear the mixing tube walls. For this inconvenience, the elevated pressure chamber experiments were carried out using liquid seeding particles.

The Mie scattering from the particles was captured as images of size 256 x 512 pixels at 8 kHz. Since the Mie scattering was imaged through a curved surface, the resulting distortion was corrected by applying a 3rd order polynomial mapping function obtained by the calibration.

Particle Image Processing

The three-component planar velocity field was calculated on the basis of two subsequent Mie scattering images taken at 8 kHz using the LaVision DaVis software package. The interrogation window size was 16x16 pixels corresponding to 0.8 x 0.8 mm^2 in physical space. A 75% overlap was chosen to get a larger number of vectors in the vicinity of the flame front (based on vaporized droplets). The distance between the wall and the first velocity vector in the radial direction was about 0.5 mm. The calibration process included correcting the images for geometrical distortion induced by the curvature of the mixing tube walls. For the current experiment, a fused-silica tube with high optical homogeneity (i.e., no lengthwise striations) was used to minimize optical defects.

Entry of the PIV laser sheet from the top of the mixing tube ensured that PIV measurements could be made near the center-body surface with a minimum of scattering. Reducing the scattering is more important with PIV than with PLIF since the laser light and scattered light are at the same frequency and so cannot be distinguished. This orientation of the laser sheet worked well at atmospheric pressure, but at higher pressure, striations in intensity appeared in the particle scattering images. These intensity striations were random in nature and were caused by the sheet passing through the swirl flame and exhaust gases. This effect increased at higher pressures owing to the larger gradients associated with the higher Reynolds numbers. Example striations in the particle scattering images are shown in Fig. 28(a). The resulting striated particle fields are problematic for PIV since they cause the cross-correlation peaks to have a two-dimensional character. Figure 28(a) shows a sample cross correlation map calculated at a location with striations and exemplifies the elongated cross-correlation function. To mitigate this effect, the intensity profile was corrected by first filtering the vertical sliding background of size 16 pixels and then applying min-max normalization filter. The resulting image had a relatively uniform particle image. A sample correlation maps for a sheet-corrected image is shown in Fig. 28. The corrected image shows axisymmetric correlation peaks, as is expected for round particle images. This operation greatly improves the quality of the resulting PIV data, as shown in Fig. 28(b).

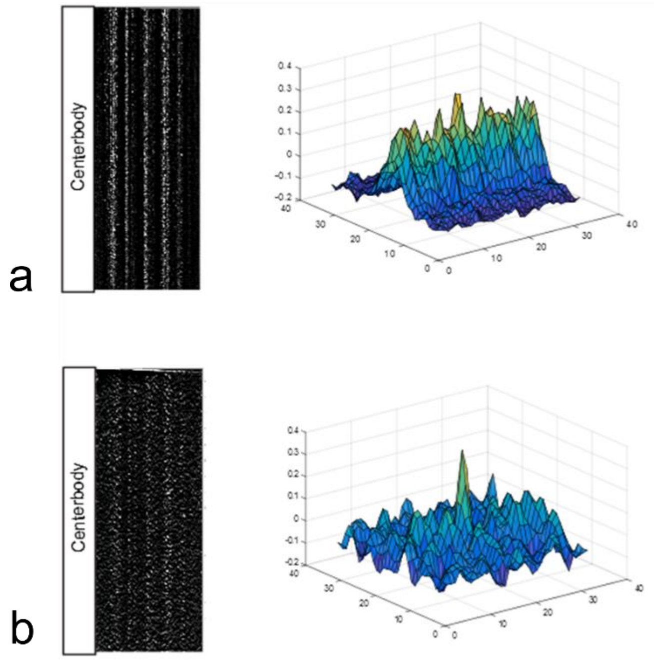

Figure 28. Striated Mie scattering image captured at 3 atm and corresponding correlation map (a) Before sheet correction (b) After sheet correction

The uncertainty in the velocity calculation for atmospheric pressure experiments is measured to be less than 0.1 m/s, whereas the stereo-reconstruction error is found to be less than 0.3 at all points in the field-of-view. For elevated pressure measurements, the maximum uncertainty bias and the stereo-reconstruction error was found to be 0.2 m/s and 0.6.

Detection of the flame front

The flame front is detected in the particle images by detecting the low scattering signal region. Since the burnt gases occupy a larger volume for a given mass, the particle density experiences a sudden dip in its value across the flame surface. This drop in particle density could be detected in particle images captured by high-speed cameras. A MATLAB code was used to extract the flame front on the basis of threshold intensity in 8x8 px windows with 75% overlap. For the particle images captured at 3 atm, striations were filtered out as described earlier. Then, a smoothing spatial filter was applied to get rid of high-frequency signals due to the discrete nature of the particle images. Afterwards, the image was binarized on the basis of a cut off intensity. Any morphological opening in the binarized image was corrected by taking the binarized version of the inverted image and then remove any gaps in the detected flame front. Then, an edge detection routine was applied to get the flame front location. It should be noted that the filtering also averages out the sub-millimeter flame structures which might exist in highly turbulent flames. Figure 29 shows the flame surface detection for hydrogen-rich flame flashback. The gamma correction of image is carried out to reveal the particles in burnt gases. It can be seen that the flame edge detection routine is successful in detecting wrinkled flame profiles.

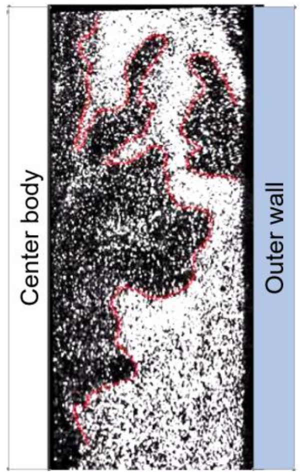

Figure 29. Flame edge detection on the basis of seeding particle density

Determination of flame front at elevated pressure remained challenging, particularly due to the presence of striations in the flow field. These striations were dynamic in nature and would cause the local fluence of the laser to low in certain parts of the particle images. A sample particle captured in an elevated pressure flame is shown in Fig. 30. In the regions marked with the red ellipse it is difficult to mark the flame surface profile.

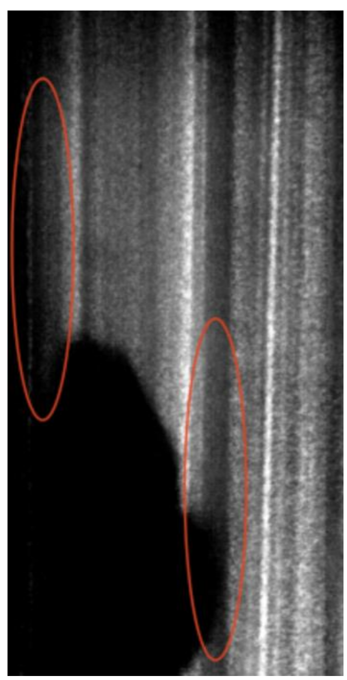

Figure 30. Striated particle image during the elevated pressure flashback of methane-air swirl flames.

Thus, the striations in the particle images affect not only the PIV as discussed in the previous subsection, but they also affect the determination of the flame front. This issue becomes even severe with hydrogen-rich flames at elevated pressure since the flame wrinkling is very strong in the hydrogen-air flames.

5. Stratified Flame flashback

In this chapter, we discuss the global propagation behavior of stratified swirl flames and the flow-flame interaction during flashback. The flashback experiments have been conducted at pressures up to 5 atm and the range of Reynolds number (based on the hydraulic diameter) is within the range 2×10^3 to 3.3×10^5. The level of stratification in the mixing tube is kept at its maximum, which means that for all flashback runs fuel is injected through the ports on the swirler vanes.

5.1 Global behavior of stratified flame flashback

5.1.1 Flame stabilization behavior

In fully premixed flashback the flame starts from a stable swirl position, propagates upstream, and stabilizes in the wake of swirler vanes. For stratified flame flashback, the flame can also stabilize on the swirler vanes, but can also stabilize aerodynamically further up in the mixing tube. These different stabilization modes are illustrated in Fig. 31. Images shown in this figure were captured with a point and shoot camera (Samsung WB350F) which was mounted outside the pressure chamber to capture the real-time video of flashback. In Fig. 31(a), a stable stratified swirl flame is shown, which stabilizes in the combustion chamber as expected for normal operation of the combustor. The appearance of this flame is similar to the premixed swirl flames in which the swirling flame stabilizes in the inner shear layer. Figure 31(b) shows the flashback stage when the flame enters the mixing tube and stabilizes at an intermediate location, downstream of the swirler vanes. At this stage the flame is noticeably louder to the ear, and the appearance of the flame is brighter as it sits inside the mixing tube. In this case, the flame stabilizes neither on the fuel ports nor on the swirler vanes. Thus, the stabilization of the flame is akin to a lifted flame, albeit in a swirling environment. We call this mode as intermediate stabilization, since the flame stops at an intermediate location in the mixing tube.

Figure 31(c) shows the flame feature which propagates farther upstream and stabilizes on the fuel injection ports. These flames are anchored robustly, and far upstream inside the mixing tube which may be catastrophic to the upstream components of the combustor. We call this mode of flame anchoring as "flameholding". The appearance of the flame is not as bright since this stage occurs only when the fuel is hydrogen-rich. The lack of CH* radicals, which emit blue luminescence, can be noted by comparing to the methane-rich case in Figure 31(b).

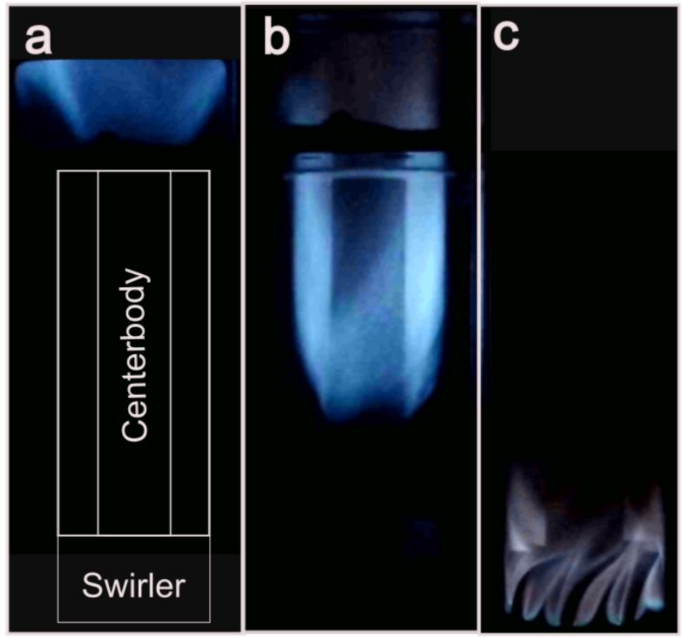

Figure 31. Different stages of stratified flames: (a) Stable in the combustor, (b) Stabilized in mixing tube after flashback, and (c) Flameholding

5.1.2. Experimental regimes

Stratified flame flashback experiments have been conducted for cases where the mean axial velocity through the mixing tube is in the range 1.1 to 4.5 m/s. Some of the experiments were conducted in the high-pressure facility, in which case the pressure was varied from 1 to 5 atm. The variation in pressure allowed us to vary the Reynolds number from $2x10^3$ to $3.3x10^5$, while maintaining similar volumetric flow rates and hence strain rates and residence times. These experiments were conducted primarily to identify the flashback regime which was described in the previous subsection.

Figure 32 shows the regime diagram of final stabilization modes after flashback has occurred. The bold curve in the plot is an approximated separation line between these two flame stabilization modes in the mixing tube. As is marked with a red dashed line, for fuel-air mixtures with >90% hydrogen content (by mole) always propagate all the way to the fuel ports on the swirler vane and the flameholding takes place. At lower Reynolds numbers, the level of enrichment required for a given equivalence ratio is lower. Similar behavior has been reported by researchers at TU Munich, who investigated hydrogen-rich flashback in a different geometrical configuration. In their case, the fuel injection was carried out on the outer wall and the flame stabilized itself on the fuel ports.

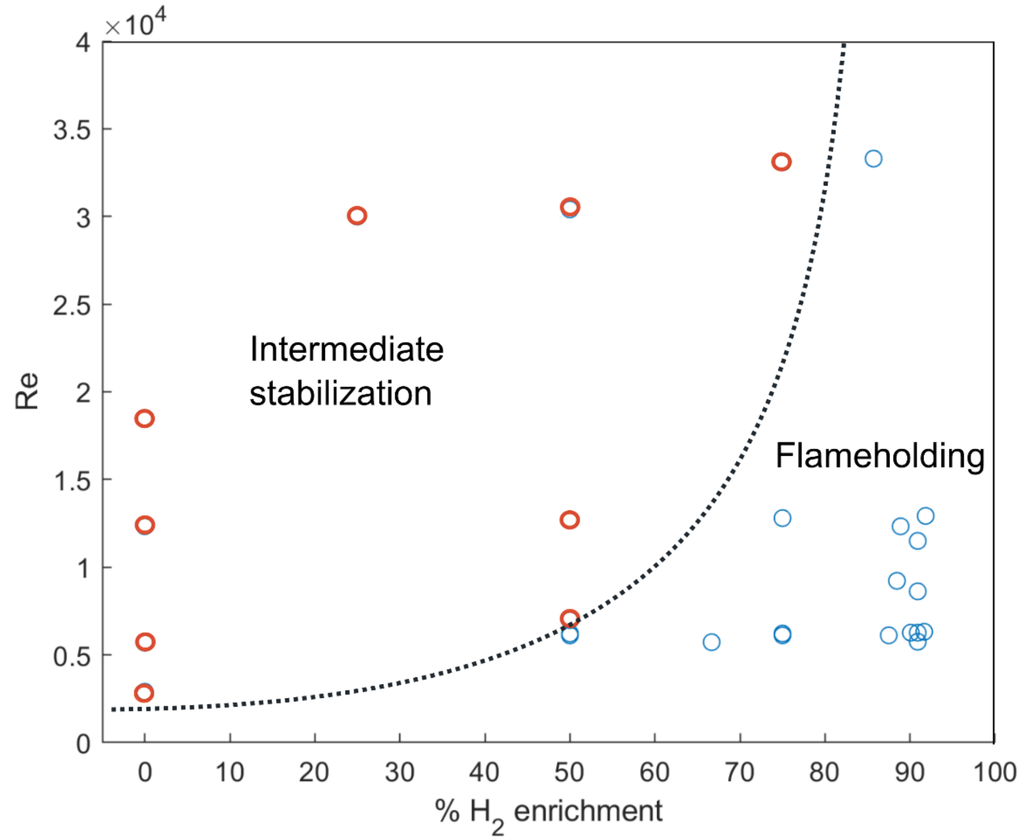

Figure 32 Regime diagram marking the mode of upstream propagation. Red circle refers to intermediate stabilization while the blue circle indicates flameholding. .

In this study we are focusing on the flow-flame interaction during flashback, rather than characterizing the conditions for which the different stabilization modes occur. Determining the global conditions is no doubt of significance to industrial applications, but is beyond the scope of this study. In this study, we focus on the flow-flame interaction and conduct detailed laser diagnostic experiments for conditions which are comparable to the premixed flashback cases described in the previous chapter.

The next subsection of this chapter is devoted to describing luminosity imaging of flashback in stratified swirl flames. We discuss the global and local behavior of the flame surface and why it is difficult to reconstruct a three-dimensional picture of the flame tongue, as we could do in fully premixed conditions.

5.1.3. Time-resolved luminosity imaging of the propagating flame

Intermediate stabilization

High-speed luminosity imaging of stratified flame flashback shows that flashback is initiated in a way that is very similar to that of the premixed case. The reason for this is that the fuel and air become progressively better mixed as they travel down the mixing tube, until they reach a nearly premixed state at the entrance to the combustor. The typical process for the initiation of flashback is that a large flame tongue swirls around the center-body, sometimes dipping down and then returning, but at some point, it continues to propagate downward along the center-body. However, after this point, the behavior of the flame for fully premixed and stratified cases is very different. For example, for the stratified case, as the flame moves upstream, at some point it reaches relatively unmixed fluid and the flame surface starts to wrinkle as has been shown in previous partially-premixed flame studies. Two instances of the flame tongue swirling around the center-body are shown in Figure 33. These luminosity images correspond to methane-air stratified flame flashback at Re_h = 6600. In Fig. 33(a), the flame tongue is an easily identifiable structure (marked as white dashed line). The flame surface is more wrinkled but the leading edge of the flame tongue can be identified and tracked. After 5 milliseconds, the flame tongue moves to the central section of the view. In premixed cases, the flame tongue retains its topology while moving in space. Furthermore, the line-of-sight integrated luminosity signal at the leading edge shows a step increase across the flame surface, which makes it possible identify the flame tip. This, however, is not the case with the flame tongue in the stratified mixture. The flame surface is more non-uniform in brightness, such as exhibiting very bright pockets, while the leading edge might be very faint, as is the case shown in Figure 33(b). In such a case, not only does the flame tip not retain its shape but it is difficult to identify the flame surface.

This situation leads us to the conclusion that not only is a stratified flame tongue different in its flow-flame interaction physics, but some basic features of the flame topology remain difficult to define. The upstream propagation of the flame stops at an intermediate location in the mixing tube, as can be noticed in Figure 33. Although the mean upstream propagation of the flame is arrested, the flame tongue still swirls around the center-body and the global features of the flame brush seem to be moving around the center-body. The flame surface fills the entire width of the mixing tube; however, this situation in not axisymmetric at any instant. The flame tongue still revolves around the center-body, even though its leading edge or the flame tip is not distinct. We did notice a distinct sound emanating from the mixing tube during flashback that may be of interest for future studies.

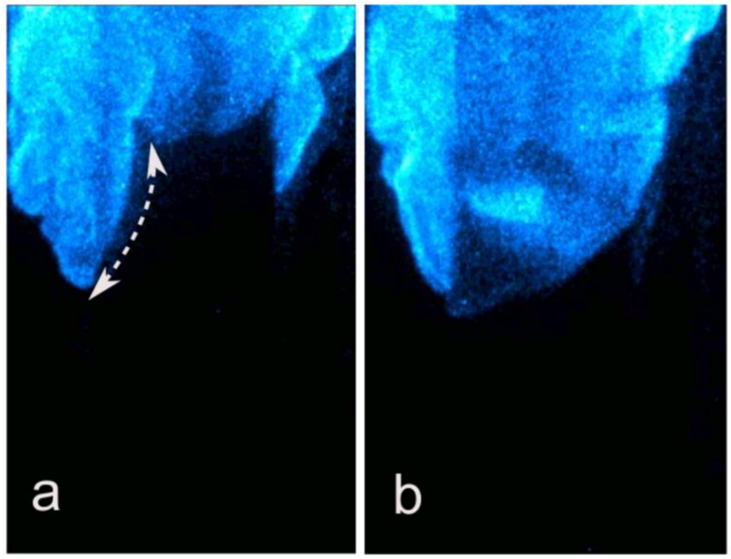

Figure 33. Two luminosity images captured 5 milliseconds apart during the stratified flame flashback of methane-air mixture. Re_h = 6600.

Flameholding

Hydrogen-rich fuel shows a higher propensity for flameholding on the fuel-ports. In the current set up, stratification is achieved by injecting the fuel through ports that are close to the outer wall. Prior to the occurrence of flashback, the swirl flame is stabilized in the inner shear layer of the recirculation zone in the combustor. The upstream propagation of the flame starts like the case of premixed flashback. A large flame tongue propagates down the center-body as it swirls around it in the same direction as the swirl flow. It has been reported that the hydrogen-rich flames have smaller radial spread than the methane-air flames for fully premixed case. This, however, is not the case with stratified flames since the flame brush fills the entire radial extent of the mixing tube. Thus, the flame brush interacts with richer fuel-air pockets in the proximity of the outer wall. The flame propagation along the center-body occurs up to an intermediate location in the mixing tube. So far, the global propagation behavior is similar to that of the intermediate stabilization mode. However, the interaction of the flame brush with the outer-wall fuel-air pockets continues. The flame brush tries to propagate into the flammable mixtures along the outer wall and seems to succeed when the flame encounters streaks of near-stoichiometric fuel-air pockets. Once it reaches the outer wall the flame starts propagating along the outer wall led by acute-tipped bright flame structures.

Figure 34 shows a sequence of luminosity images that are captured 5 milliseconds apart. The formation of a flame structure along the outer wall is marked with a yellow ellipse. In Figure 34(a), a locally bright flame structure that moves in the approach flow direction (red arrow) spreads out quickly and leaves behind acute flame structures, which anchor themselves in the outer wall boundary layer. These flame structures are pointed in the negative streamwise direction, and are similar to the small scale structures that form in the trailing side of the flame tongue during premixed flame flashback. It is interesting to notice that these structures do not get convected in the direction of the swirl. Once anchored in the outer wall boundary layer, these structure show resistance to the approach flow. During this phase, the flame structure does not seem to move. At times, these structures are washed away by the approach flow, however once a structure starts propagating upstream and anchors on one of the fuel ports, the flame anchors itself on all the fuel injection ports. This step towards flame anchoring is very fast as compared to any of the previous stages.

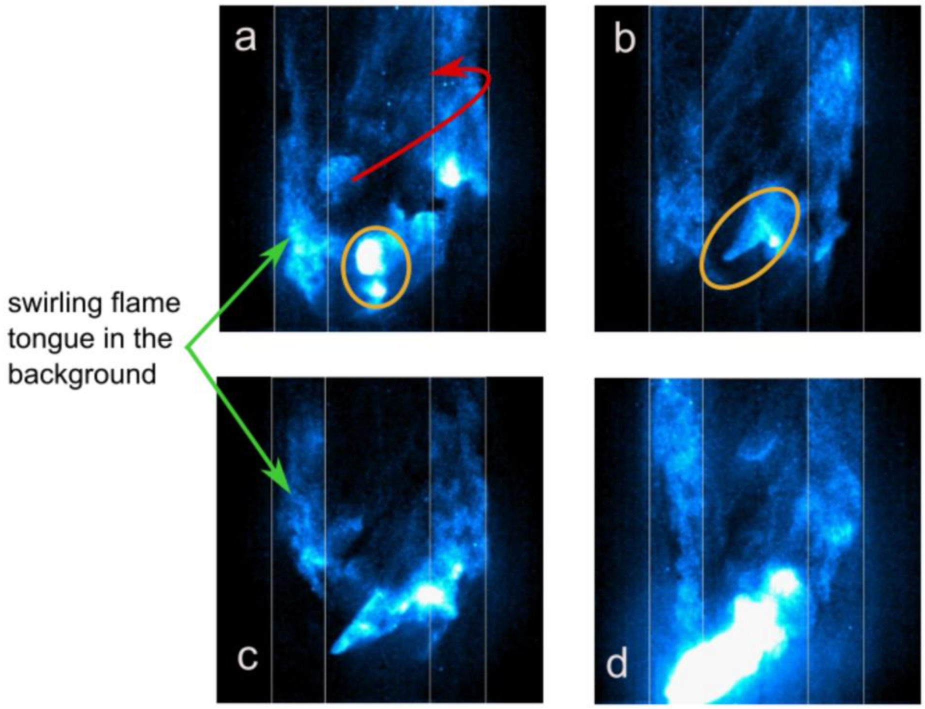

Figure 34. Propagation of flame structure on the outer wall a. bright flame structure appearance b. acute flame structure formation c. acute flame anchoring d. upstream propagation towards flameholding. Red arrow shows the direction of the approach flow.

When the flame structure does not form in the central section of the luminosity image, it is very difficult to identify the flame structure. Also, the formation of these acute structures is random. It requires multiple flashback runs until one gets to capture the propagating flame structure in the central section (center-body in the background).

Another interesting feature of stratified propagation is the simultaneous presence of the swirling flame tongue on the center-body. It is usually difficult to decipher because of its lower level of luminescence, but dim flame tongues on the center-body can be noted in Figure 34. The flame tongues are circled with an orange ellipse in Figure 34. The swirling flame tongue is on the left side of the luminosity images, although it is easier to see in the videos than these still images. It should be noted that the initial formation of the bright flame structure in Figure 34(a) occurs on the flame brush of the swirling flame. In other words, the intermediate-stabilized swirling flame in the mixing tube acts as the initiator of the propagation along the outer boundary wall.

5.2 LASER DIAGNOSTIC EVALUATION OF STRATIFIED FLAME FLASHBACK

Based on our observations from luminosity images, we already know that the fuel-air distribution in the approach flow affects the characteristics of the flame surface. Hence, in this work, we first assess the fuel-air mixing in the mixing tube and then report time-resolved PIV data.

We employ planar laser-induced fluorescence imaging (PLIF) with acetone as the fuel tracer. For methane-air mixing, we inject acetone-seeded air with the same flow rate as that of methane during flashback. The mixing characteristics of the methane are assumed to be similar to that of acetone-air due to their comparable density and diffusivity characteristics. The PLIF images are captured at 10 Hz, and thus insights provided by these images are not time-resolved in nature. However, these images can provide important statistics for methane-air mixing in the annular swirling flow. The distribution of equivalence ratio in the mixing tube was determined by first calibrating the signal at the exit of the mixing tubes as representing the "pure" fuel state (note that it is actually composed of a mixture of acetone and air). This signal was then used to normalize the PLIF signal at all imaging locations, and from this normalized signal the equivalence ratio could be computed.

5.2.1 Stratified Methane-air swirl flame flashback

Fuel-air mixing

In this subsection, we report the fuel-air mixing characteristics as assessed using acetone PLIF images. The hydraulic-diameter Reynolds number is kept at 6600, while the global equivalence ratio is kept at 0.63. The field of visualization extends from z = -50 mm to z = -80 mm (negative signifies the upstream location). At these flow conditions, during the reacting-flow experiments, the flame propagates into the mixing tube and attains intermediate stabilization within the field of view. With an assumption, that the flame's presence in the mixing tube does not affect the fuel-air mixing upstream of the flame. It is reasonable to assume so since the intermediate stabilization occurs at about 60 to 65 mm upstream of the mixing tube, whereas the fuel is injected about 120 mm upstream of the fuel injection ports. The distance between the fuel ports and the flame brush is thus about 70 nozzle diameters downstream as measured from the fuel-injection ports. It should be noted that fuel-air mixing is affected by multiple other factors such as jet-jet interactions, jet-wall interactions, jet-vane interaction and the swirling action of the swirler. In such a case, it is not feasible to compare the mixing with any canonical studies. Phenomenologically, one can say that as the fuel-air pockets move along the flow, they mix primarily due to molecular and turbulent diffusion. Schmidt number, the ratio of kinematic viscosity and the molecular diffusivity for methane-air and acetone-air is 0.99 and 1.5, respectively. Thus, by keeping the same Re and similar Schmidt numbers, one can argue that the mixing characteristics can be assessed reliably.

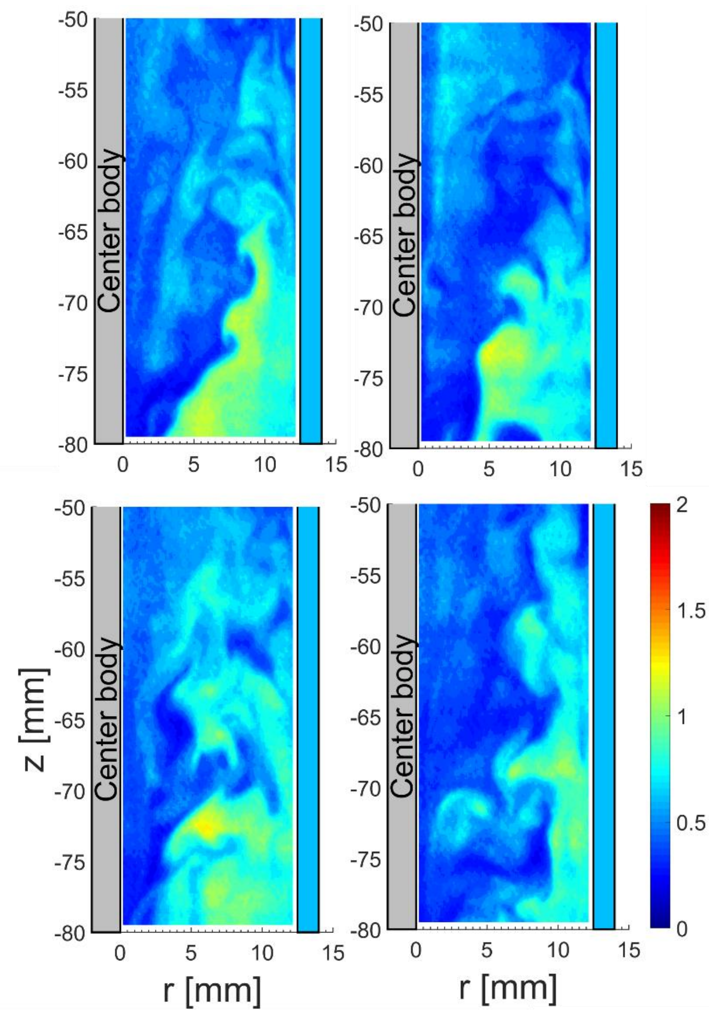

Figure 35. Instantaneous PLIF snapshots showing the distribution of equivalence ratio at flashback-equivalent conditions. Re_h = 6600

Figure 35 shows instantaneous statistically-uncorrelated PLIF images of fuel-air mixing. The flow close to the center-body is predominantly fuel-lean. Stoichiometric and fuel-rich pockets can be noticed in the flow close to the outer wall. This confirms that the fuel-injection strategy of positioning the fuel-injection ports away from the center-body leads to an inhomogeneous equivalence ratio distribution. The intermittent presence of fuel-air pockets close to the center-body can be attributed to the swirl and turbulence in the mixing tube flow.

Figure 36 shows the mean distribution of the equivalence ratio in the mixing tube. At z = -80 mm, the equivalence ratio at the center-body is very lean ($\phi \sim 0.3$) while the flow at the outer wall is richer ($\phi \sim 0.9$). The lean and rich flammability limits for methane-air mixtures are 0.5 and 1.7 respectively, and near these limits the flame speed becomes small. Thus, in a mean equivalence ratio field, the propagating flame would not be able to reach z = -80 mm. At z = -68 mm there is a sudden change in the mean fuel-richness of the flow, which can also be noted in the instantaneous PLIF images in Figure 35. The reason behind it may be the orientation of the streamlines, which move out of the plane of the laser sheet; thus, any fuel-rich pocket would move out of the measurement plane. The three-dimensionality of the flow also makes it difficult to comment on the length-scales of the fuel-air pockets.

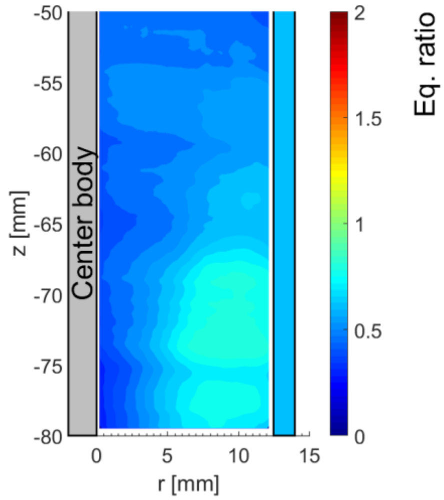

Figure 36. Mean distribution of equivalence ratio during methane-air mixing at Re_h = 6600, Global equivalence ratio = 0.63.

Flame-flow interaction during the methane-air flashback

As discussed in the previous subsection, as the flame propagates upstream along the center-body it encounters a lean premixture embedded with intermittent fuel-rich pockets. Near the lean flammability limit, the flame luminosity becomes very low, which makes the identification of the flame surface challenging. In left and right sections of the field of view, the line-of-sight integrated signal is affected by the flame curvature. To explain this issue, we show two luminosity images captured during stratified flame flashback in Figure 37. The images Figure 37(a) and (b) show the same luminosity image, except a gamma correction has been applied to Figure 37(b).

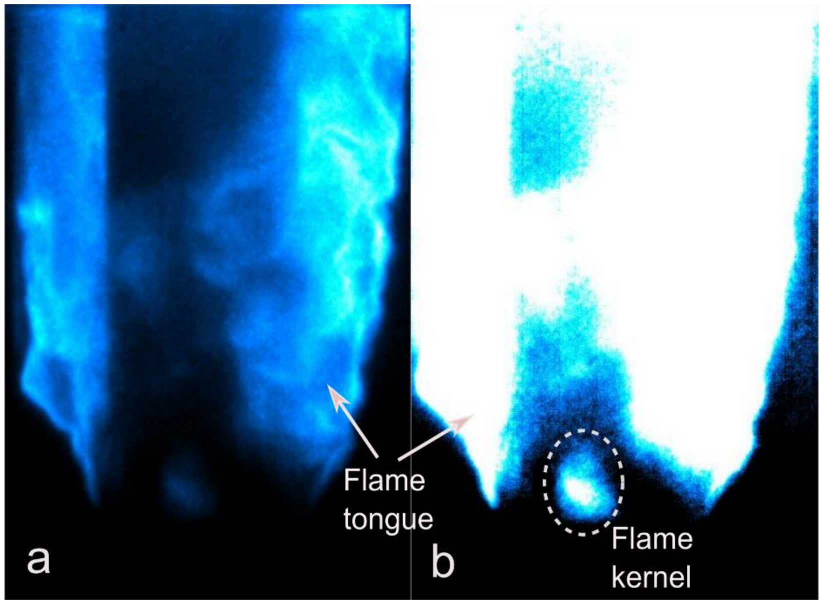

Figure 37. Luminosity image captured during methane-air stratified flame flashback (a) Gamma = 1, (b) Gamma = 0.3

In Figure 37(a) the luminosity from the flame surface is captured while the region close to the leading edge of the flame tongue is not visible. The brightness on the flame brush is due to the fuel-rich pockets burning at regions away from the center-body. In such a case, any interesting feature at the leading edge is easy to miss. On the other hand, once gamma corrected to observe the leading line of the flame surface, we notice a flame kernel near the flame front. It appears to be disconnected from the flame surface, but it cannot be so, since the ignition of this kernel, which is at room temperature before burning, is not possible without an ignition source. Any possibility of auto-ignition does not exist since the fuel-air premixture is not preheated. This argument suggests that even though there is nearly zero luminosity around the flame kernel, there should be a flame surface in its vicinity that ignites it, as it moves downstream in the mixing tube. This raises the question whether we can detect an ultra-lean flame that lies close to the center-body.

In this subsection, our discussion focuses on how the apparent flame kernels affect the flame surface and the flow upstream of it. The leading regions of the flame surface – in the absence of the fuel-rich pockets -- should play little role in blocking the approach flow since the flame resides in barely-flammable lean regions. Hence, in the subsequent paragraph, we discuss the interaction of the bright flame structures and approach flow.

Figure 38 shows the simultaneous luminosity and velocity field upstream of the flame surface. Figure 38(a) and Figure 38(b) are spaced by 3 milliseconds while rest of the images are captured 1 millisecond apart. Figure 38(b) – (d) tracks a bright flame structure, circled in yellow, which crosses the laser sheet. The white region in the velocity contour plot indicates the presence of flame products that vaporize the PIV seed particles. The effect of the bright flame structure on the velocity field is evident as it crosses the laser sheet. Regions of negative axial velocity are found upstream of the flame front during the time that the structure crosses the laser sheet. Simultaneous out-of-plane velocity (not shown) is positive, which shows that these flame structures deflect the incoming flow rather than causing flow reversal.

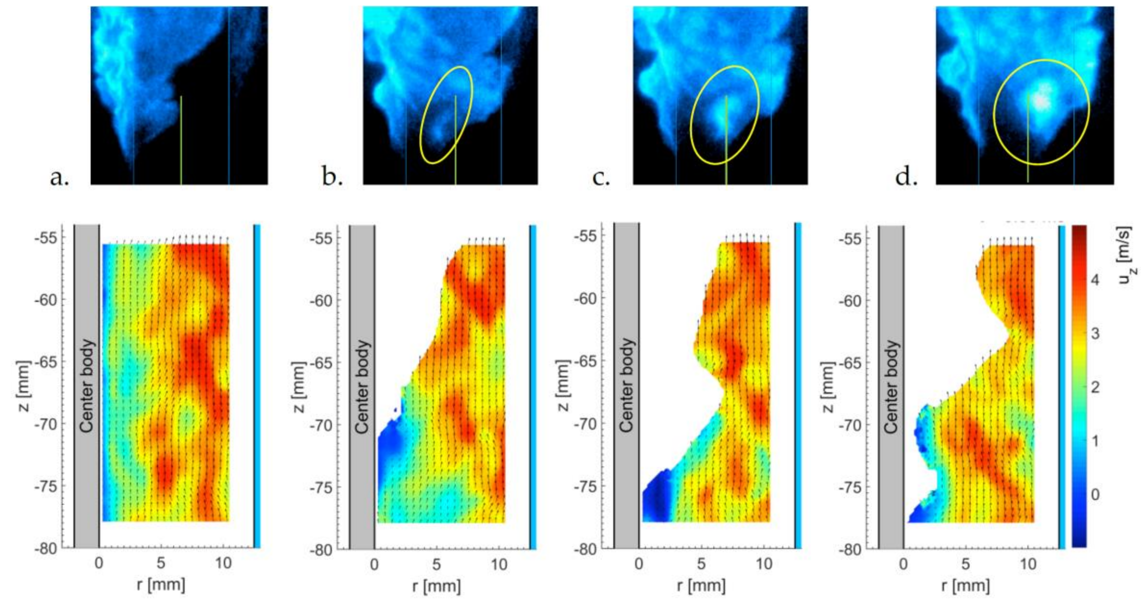

Figure 38. Chemiluminescence and the axial velocity fields at time instants: (a) t_0, (b) t_0+3, (c) t_0+4, and (d) t_0+5 ms. Green line in the chemiluminescence images shows the position of laser sheet. Evolution of a flame structure is marked by yellow circle.

Prior to the flame structure crossing the laser sheet, the planar profile of the flame was not wrinkled. However, as noted in Figure 38(c) and (d), the flame kernel wrinkles the flame surface and at the same time applies a strong blockage effect on the approach flow. This structure imposes negative axial velocity on the approach flow. It should also be noted that despite imposing very strong blockage effect on the approach flow, the bright flame structure does not change its motion. Instead it keeps moving along its spiral path towards the mixing tube exit. The apparent lack of deflection of the bright flame structures' path tells us that in global upstream motion of the flame brush during flashback, a single flame kernel does not contribute to the propagation dynamically. Instead, it moves along the spiral path around the center-body. Along its way out, the flame structure burns out depending on its length scale. The burning out of this flame structure is identified by the decrease in luminosity of the flame structure.

The chemi-luminescence signal captured in these images are line-of-sight integrated and have a strong dependence on local ϕ. A local variation in ϕ imposes variation in local flame speed, stretches the flame surface and increases the flame curvature. The presence of bright flame structures seems to result from the presence of locally fuel-rich pockets in the flow, which is consistent with the non-reacting PLIF measurements. To confirm this hypothesis, acetone PLIF measurements were taken for reacting flows as well. However, seeding of fuel flow with acetone affected the flashback limits for a given bulk velocity and required smaller fuel flow rates to trigger the flashback.

Figure 39 shows two normalized PLIF snapshots capturing the flame brush during a stratified-flame flashback event. The flame front can be identified as the region of sharp decrease in PLIF signal, which occurs owing to the pyrolysis of acetone in the preheat zone of the flame. The regions of large curvature, such as the cusps (in red ellipse, Figure 39(a)), are associated with a sharp change in the spatial distribution of ϕ. This observation confirms the role of mixture variation in wrinkling of the flame brush of the flashing back stratified flame; however, we are not able to map the PLIF signal to equivalence ratio owing to pyrolysis and temperature variations that affect the acetone PLIF signal. Instead, the pixel intensity was normalized with the maximum pixel value in the visualized region. After normalization, the region with maximum PLIF signal should correspond to fuel-rich regions. If we correspond these fuel-rich regions with those in the non-reacting flow, the local equivalence ratio in these pockets should correspond to $\phi \sim 1.1\text{-}1.6$ for the methane-air mixture. As we discussed in the literature review, this range of equivalence ratio corresponds to the unstretched laminar flame speed of 0.2 to 0.3 m/s. Thus the flame wrinkling shall occur depending on the local equivalence ratio gradient. If the pocket is near-stoichiometric, it would induce positive curvature on the flame surface. On the other hand, if the fuel-air pocket in near the flammability limits then the flame surface would have little propagation in those regions. The resulting variation in local flame speed thus modulates the flame surface. There should also be additional effects that come into play, such as in a back-supported or front-supported flame environment, but these details are difficult to comment upon.

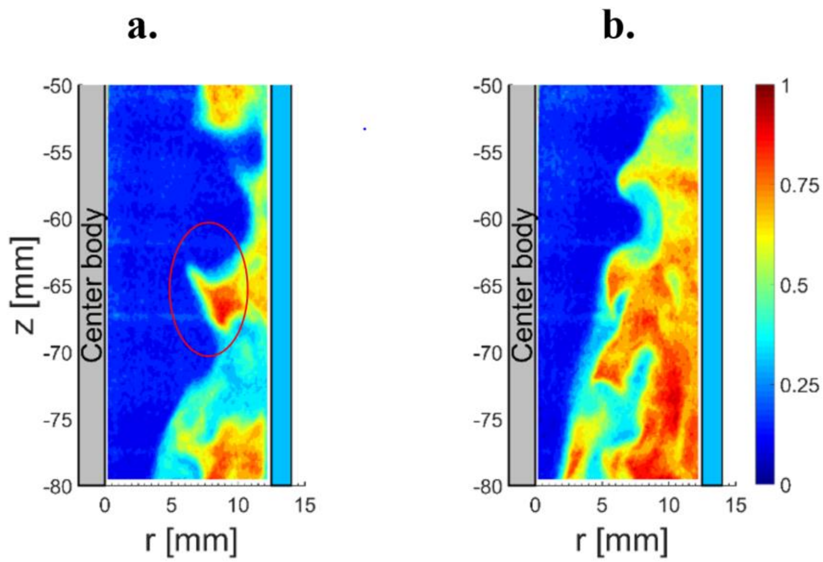

Figure 39. Normalized acetone PLIF signal captured during a flashback event. The different uncorrelated example images are shown.

5.2.2 Stratified hydrogen-rich swirl flame flashback

Hydrogen-enrichment of fuel leads to new pathways for flames to propagate, as we have discussed previously. In this section, we analyze hydrogen flashback behavior for the case with the same mean axial velocity of 2.5 m/s and with hydrogen enrichment of 87% by mole.

The global equivalence ratio is maintained at 0.4. First, we assess the mixing behavior of the fuel and air.

Mixing behavior

Acetone PLIF was also used to investigate the mixing characteristics for the case of stratified flashback with enriched-hydrogen fuel. However, in contrast to the work above, the acetone was seeded into helium to create a non-reacting surrogate that had a density that is closer to that of the enriched hydrogen fuel. Helium is seeded with acetone by passing through the acetone bubbler. Instantaneous PLIF images for these runs is shown in Figure 40.

A comparison of Figs. 35 and 40 indicates that the mixing behavior is qualitatively similar to that of the methane-fuel case. There are fuel-lean yet locally-richer fuel-air pockets spread across the mixing tube. The concentration and relative size of these pockets are large close to the outer wall; however, there is an intermittent presence of fuel-air pockets close to the center-body boundary layer.

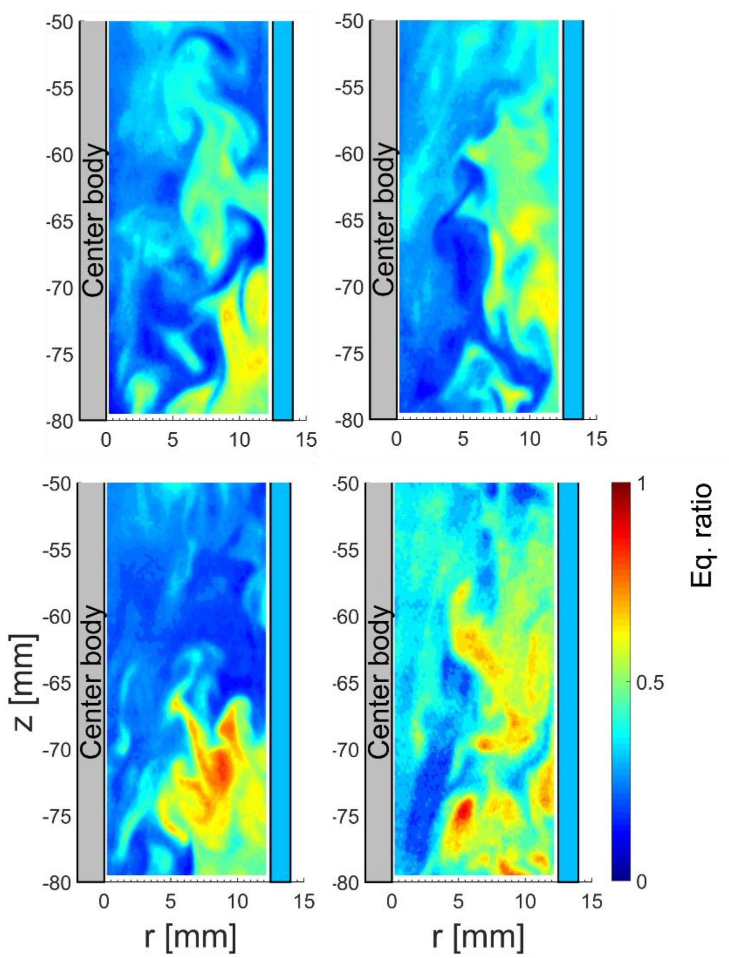

Figure 40. Instantaneous equivalence ratio fields for helium-air mixing Re_h = 6300. Four uncorrelated snapshots are shown.

The mean of 900 instantaneous images is shown in Figure 41. The mixing behavior of the mean is also similar to that of methane-air mixing, except that the equivalence ratio values are different. For the case of hydrogen-rich fuel, the equivalence ratio does not reach stoichiometric in the mean, which simply reflects the lower global equivalence ratio used. Also, instantaneously, there are pockets of near-stoichiometric mixtures in the flow.

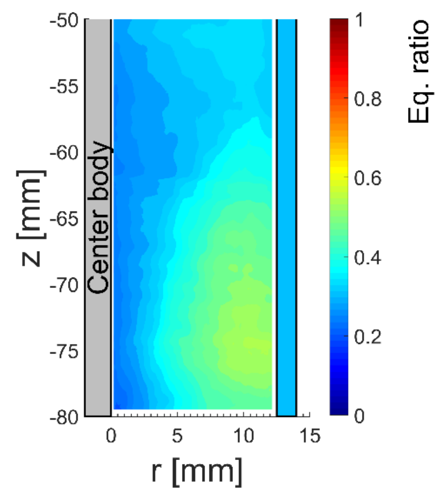

Figure 41. Mean equivalence ratio distribution in the mixing tube. Re_h = 6300

The hydrogen-air mixture, even though fuel-lean in terms of equivalence ratio, is still very reactive as compared to stoichiometric methane-air mixtures. The lean flammability limit equivalence ratio for 87% hydrogen-methane mixture has a lower flammability limit of 0.11. These limits encompass almost entire visualized region in the mixing tube. In flammable regions, the unstretched laminar flame speed of hydrogen-air is as high as 3 m/s for near-stoichiometric fuel-air pockets. These fuel-air pockets occur frequently in the regions close to the outer wall as shown in Figure 40, thereby increasing the likeliness of flame propagation along the outer wall.

Time-resolved luminosity images and simultaneous PIV

We observe that hydrogen-rich flashback occurs in two steps. The first step is the propagation along center-body boundary layer in a way similar to that of the fully premixed flame. The flame starts from a stable condition where it is anchored in the inner shear layer of the combustor. Upon triggering the flashback, it propagates upstream through the boundary layer of the center body. In a manner similar to the intermediate stabilization, the flame tongue rotates around the center-body. The flame brush is broad enough to maintain interaction with the outer wall. During this interaction, the flame surface propagates to the outer wall and begins to propagate down it. It should be noted that the flame's existence along the outer wall is not favored by the swirling action since it leads to the low-density fluid along the outer wall. The centrifugal force acts radially outward and so the low-density gases on the outer wall is inherently unstable. Still, the propagation of the flame surface along the outer wall occurs, primarily due to the fast chemistry associated with the richer mixtures at the outer wall. In Figure 42 we show the first definitive evidence of flame propagation along the outer wall using simultaneous time-resolved PIV and luminosity. The framing rate for these measurements is 4 kHz.

Figure 42(a) shows an instant when the flame along the center-body and the outer wall are on the either side of laser sheet (green). In 4.25 milliseconds the flame on the center-body revolves around the center-body and crosses the laser sheet. At the same time, the flame structure on the outer wall also crosses the laser sheet in the opposite direction. At this instant, the outer wall and the center-body flame structures share the same azimuthal location. The propagation of the outer wall structure occurs as an acute flame tip shedding the burnt gases as bright flame structures. The burnt gases, which are low in density, cannot sustain themselves in the vicinity of the outer wall. Thus, immediately after getting burnt, these gases form a puffy tail-like structure in the wake of the leading point of the propagating flame surface. In Figure 42(c), the flame on the center-body has crossed the laser sheet and is on the other side of the annulus. At this stage, the acute flame tip which is anchored in the outer wall boundary layer, starts propagating upstream. During this process, the single flame structure bifurcates into 2 to 3 flame structures approaching the fuel-injection ports.

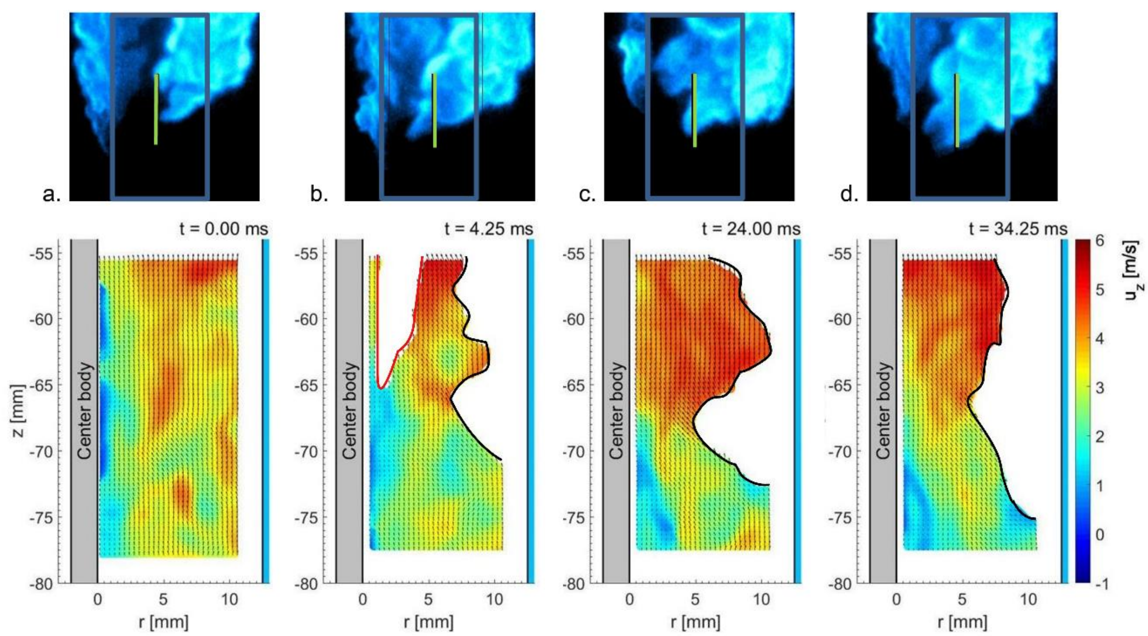

Figure 42. Chemiluminescence images and simultaneous axial velocity fields at different time instances during flame propagation along the outer wall boundary layer. White region in the velocity shows the burnt gas region.

While propagating, we expect the outer flame structure to apply blockage to the approach flow. These flame structures, which push the approach flow in the negative streamwise direction, can apply blockage to reverse the flow at the flame tip. To capture this effect, the laser sheet needs to be imaged very close to the outer wall of the mixing tube. The curvature of the mixing tube makes it difficult to capture this detail. In the results reported here, we could get PIV data up to 2 mm away from the outer wall. Thus, any portion of the flame and the flow within 2 mm of the wall could not be captured. However, the blockage from the flame structure is apparent in Figure 42(d). Just upstream of the flame tongue (z = -77 mm, r = 10.5 mm), the blockage effect from the flame reduces the axial velocity to ~ 1 m/s, as marked by local light blue background.

Another interesting aspect of this propagation is the flow-flame interaction. The flame structure on the center-body keeps swirling while anchored at an intermediate location. This swirling flame can cause a sweeping effect in the azimuthal direction, similar to the one discussed in previous chapter. On the other hand, the outer flame structure, which is primarily controlled by the equivalence ratio distribution upstream of it, also interacts with the flow by pushing in the opposite direction. Now, inside the mixing tube, these two flames move in opposite swirling directions. The flow that is affected by the flame on the center-body can also interact with the flame on the outer wall, which can cause a three-way interaction. To ascertain this would require simultaneous multi-plane measurements, however, this was not possible with our current experimental setup.

To further understand the propagation along the outer wall, we describe the flame propagation in two stages: (1) flame anchoring on the wall, and (2) flame advancement along the wall. Flame anchoring on the wall can be defined by attachment of acute flame tips on the outer wall. In this process, the flame does not move but resists getting convected with the approach flow. At times, acute flame structures anchor themselves and thus resist being convected by the upstream flow. The flame advancement stage starts when the flame structure starts propagating upstream. In this phase, either the flame structure bifurcates into two similar structures or it remains on the streaks of stoichiometric mixture (most reactive mass fraction) and advances till the flameholding occurs.

PIV runs were conducted in an atmospheric-pressure burner with alumina seeding particles. Alumina particles do not get consumed in the flame and so it is possible to obtain velocity measurements in the burnt gas regions. In previous work, the 2D dilatation has been found to agree well with the flame surface. Theoretically, the three-dimensional divergence value should be zero everywhere except for the flame surface. Also, the larger the volume generation per unit volume, the larger would be the divergence. Thus, it is also an indirect indicator of heat release, assuming that the entire heat release acts to generate volume. With this idea, we use the 2D divergence value as the marker of heat release. Another marker of heat release in stratified flows is luminosity, however deriving any quantitative measurement is beyond the scope of current work.

Figure 43 shows two instances during the flame anchoring phase. At first there is no acute structure on the wall, however a bright flame structure crosses the laser sheet (shown with light green). In Figure 43(a), in the velocity field, the flame surface is marked with a white line. Determination of the flame surface was accomplished by looking for large changes in the local particle density. It can be noted that the flame surface agrees well with the 2D dilatation, but only in the upstream portions of the flame surface.

In previously reported work on fully premixed flames had found these peaks of large 2D dilatation all along the flame surface. In Figure 43(b), even though the flame surface exists in the laser sheet plane, there were no distinguishable peaks in the 2D dilatation map. One can correlate the absence of bright flame structure in the laser sheet plane with the absence of peaks in the 2D dilatation map. This observation agrees well with the idea that the bright flame structures are associated with large heat release – and hence with large three-dimensional dilatation which reflects in the 2D dilatation maps. With this argument, the large 2D dilatation values at the upstream locations of the flame structure indicates that the heat release on the flame structure is not the same all along the surface. The axially-upstream side of the flame structures have large dilatation than the axially-downstream side of the flame tongue. This observation may be an outcome of environment around the propagating flame structure. These acute flame structures move through the stratified fuel-air mixture, propagating along the regions of the most reacting mixture fraction. This structure should have a relatively richer and a relatively leaner fuel air mixture on either side of it. Hence, the sides of these structures – visualized as the axially upstream and downstream side in Figure 43 should have different levels of dilatation. This should also have reflected in the luminosity imaging; rich and lean sides of the flame structures should have different levels of luminosity. However, no such evidence was found in the luminosity images. The fact that there is another dim flame structure in the background (revolving around the center-body), any comment on the variation of luminosity across a flame structure is difficult to make.

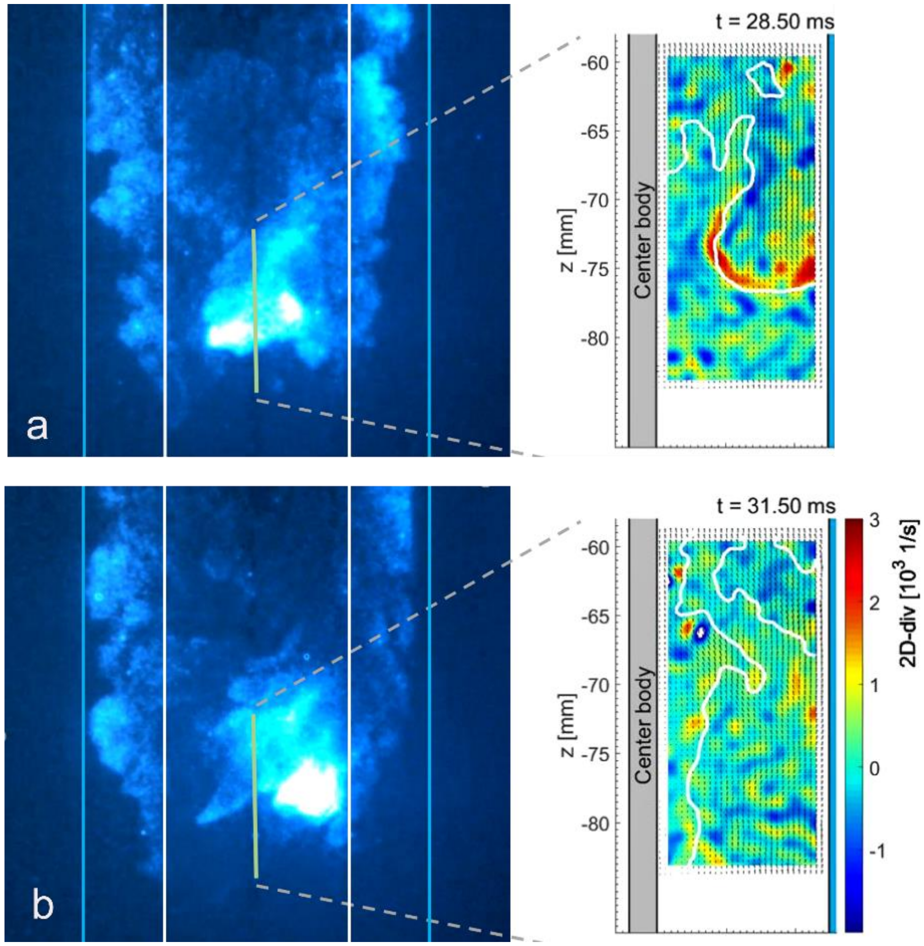

Figure 43. (a) Bright flame feature crossing the laser sheet and simultaneous 2D divergence field, (b) Formation of acute tipped flame structure on the outer wall

In Figure 43(a), the bright flame structure in the luminosity image corresponds to the region of high 2D dilatation in the PIV data. In Figure 43(b), the bright structure moves downstream, while the acute-tipped flame structures stay as it is. In the PIV image there is no sign of large dilatation in the vicinity of the flame surface.

For the flame advancement stage, we show three instantaneous PIV images along with the luminosity (Figure 44). In these images, the flame surface exists along the center-body boundary layer as well as along the outer wall. In Figure 44, the regions of large divergence are associated with the flame on the center-body and not on the outer wall. However, at subsequent times, this large divergence shifts toward the outer wall. Simultaneously, the bright flame structure now interacts with the outer wall and assists in making progress in the upstream direction.

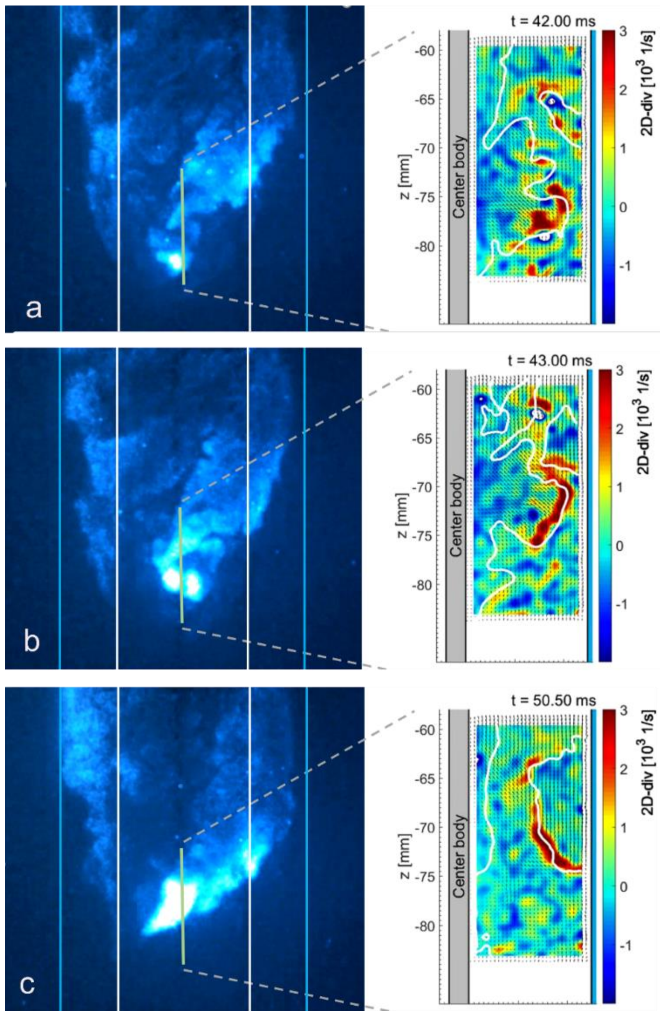

Figure 44. Simultaneous luminosity images and 2D divergence maps. Regions of large divergence correspond to the bright flame structures crossing the laser sheet.

If we associate the luminosity and the dilatation value with the heat release, these bright flame structures are essentially sources of large heat release. Thus, when these structures interact with the boundary layer, they allow the flame to anchor on the outer wall. If they occur in tandem, or in the vicinity of the stoichiometric mixtures, they can assist in upstream propagation of the flame.

5.3 Effect of elevated pressure

In the current study, elevated pressure flashback runs were conducted at the same mean axial velocity as that of the atmospheric pressure runs. Thus, an increase in pressure results in a proportional increase in the Reynolds number. In this work, we report flashback behavior for methane-air stratified flames at 3 atm and Re_h = 18,400. As in the atmospheric-pressure cases, acetone PLIF was to assess the fuel-air mixing behavior in the mixing tube under non-reacting conditions. For example, Figure 45 shows instantaneous images of equivalence ratio that were derived from the acetone PLIF data.

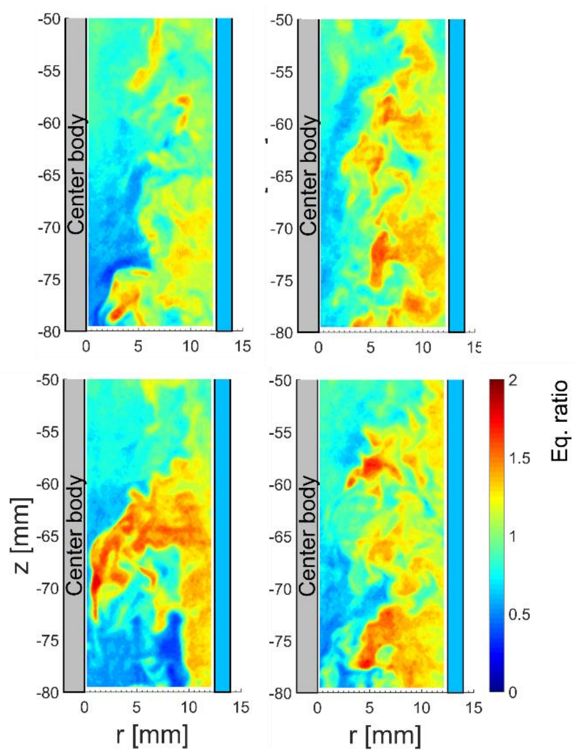

Figure 45. Instantaneous PLIF images showing the small-scale fuel-rich structures in the flow. These images correspond to methane-air flashback at 3 atm. Re_h = 18600 ϕ = 0.85

Pressure can affect flame propagation characteristics by affecting the reaction chemistry and by increasing the turbulence through the higher Reynolds number. In our discussion on stratified flow-flame interaction, pressure is likely to be important owing to both effects. The effect of turbulence in the flow is apparent in the instantaneous PLIF images as captured at 3 atm. There are multiple small-scale (sub-millimeter) structures that were not present in atmospheric pressure runs. For methane-air mixtures, the laminar flame speed decreases with an increase in the pressure. This reduction in the flame speed is consistent with our observation that the flashback limit increased at elevated pressure. At 3 atm, flashback was triggered at ϕ = 0.85, as compared to 0.63 at 1 atm. At 3 atm, once flashback occurred, the flame would always stabilize on the swirl vanes. Furthermore, the flame brush was wrinkled, bright and filled the mixing tube. The flame front was found to be marked by small-scale flame structures.

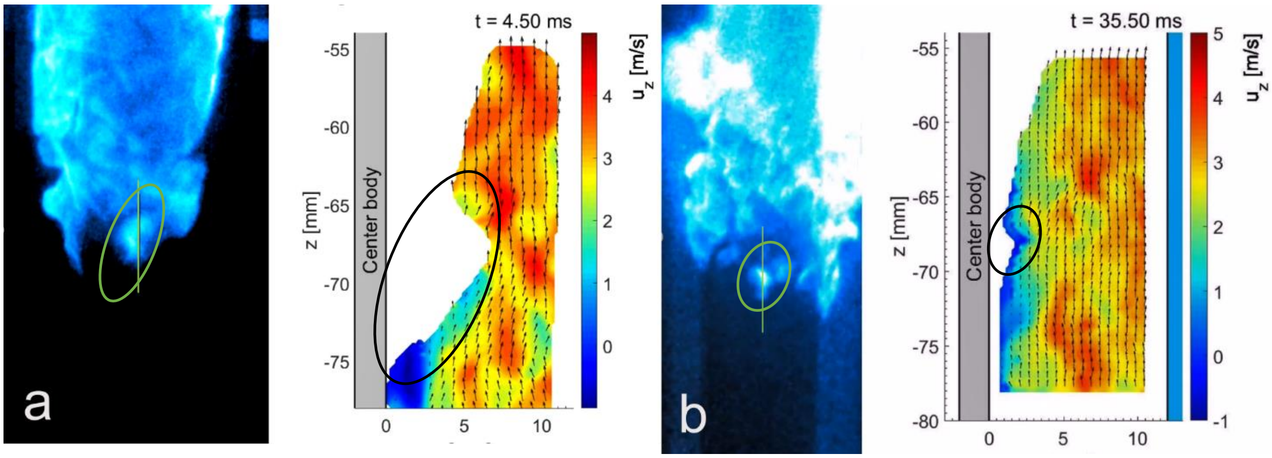

Figure 46. Interaction of the flame surface and fuel-rich pockets in the approach flow. (a) 1 atm, and (b) 3 atm. The orange ellipse mark the luminosity signal from bright flame structures. Black ellipse show corresponding effect on the flame surface

Figure 46 shows two instants from methane-air flashback events at 1 atm and 3 atm. Luminosity is shown on the left and PIV on the right. These two instances are comparable since in both the cases the fuel-air pocket interacts with the flame surface. At atmospheric pressure, the fuel-air mixtures are usually not fine scale, thus the interaction between the flame tongue and the fuel-air pockets alters the topology of the flame surface significantly. It can be seen that these pockets can have a strong effect on the approach flow as well. On the contrary, at 3 atm, the fuel-air pockets are smaller scale (ellipse in Figure 46(b)), and seem to have lower impact on the approach flow. Figure 46(b) shows an instant at 3 atm when the rich fuel-air interacts with the flame surface. It can be seen that there was very little change to the flame surface (marked with black ellipse).

Elevated-pressure hydrogen rich flashback still follows the flashback behavior as described for the atmospheric pressure case. Flashback experiments were conducted at 3 atm, with global equivalence ratio of 0.3. Hydrogen enrichment was kept at 86%. Similar to the 1 atm case, the flame propagated along the center-body and then the flame switched to the outer wall.

The propagation along the outer wall occurred in a similar way as that of at atmospheric pressure; however, the flame along the outer wall was characterized as a wider flame tongue, which is similar to observations of channel-flow flashback.

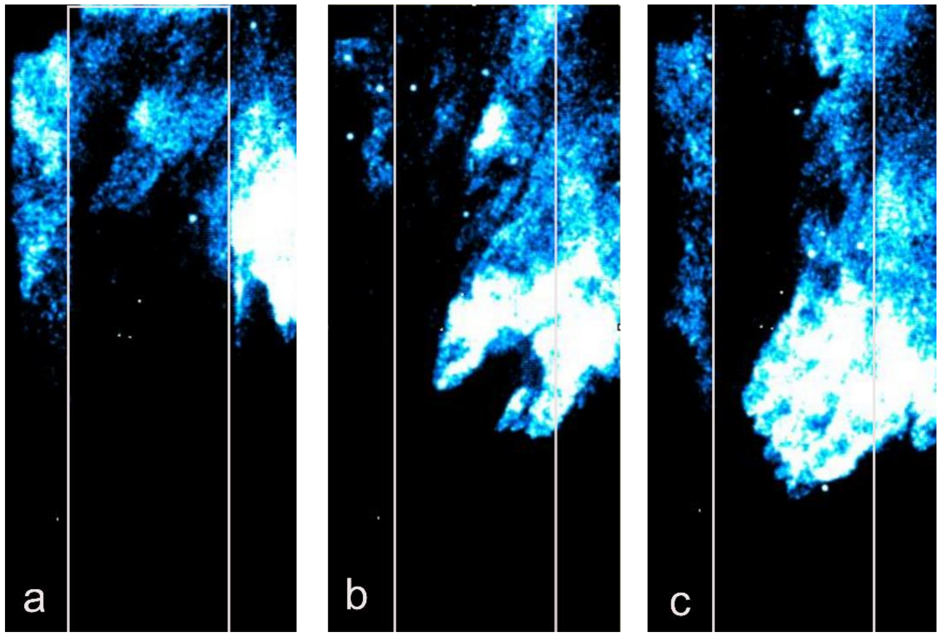

Figure 47. Luminosity images captured during hydrogen-rich flashback at 3 atm (a) t_0, (b) t_0 + 12 ms, (c) t_0 + 14 ms; Re_h = 18600 ϕ = 0.3

Figure 47 shows three instants during a hydrogen-rich flashback event. In Figure 47(a) the flame brush clings to the outer wall of the mixing tube. Flame anchoring occurs in a similar way as that of the 1 atm case. Two acute flame tips were found to propagate along the outer wall in Figure 47(b). These acute tips are also a bit wider (by a few millimeters). Interestingly the advancement towards the fuel injection ports occurs as a wide band (≈10mm) instead of the acute-tipped flame feature. This suggests that the acute-tip structures primarily anchor the flame in the outer wall boundary layer and act to spread the flame in the approach flow such that a wide flame tongue could be formed. Simultaneous PIV measurements could not be taken for elevated pressure measurements due to limited number of experiments which could not capture the flame tongue propagation within the field of visualization.

6. Summary of the Experimental Program

Stratified flame experiments were conducted for a wide range of Reynolds numbers. The level of hydrogen enrichment was varied up to 87%. The global propagation behavior of the flame tongue was studied and two modes of flame stabilization in the mixing tube. The first mode, intermediate stabilization, corresponded to the case when the propagating flame stops at an intermediate location in the mixing tube, and keeps swirling without making a continuous upstream movement. The overall appearance of the flame surface was characterized with a bright flame brush and a relatively dim upstream flame surface. At the leading side of the flame tongue, intermittent bright structures were noted. The second mode of flame stabilization is characterized by the anchoring of the flame on the fuel ports. In this mode, the flame propagation occurs along the outer wall and it continues until the flame is stabilized on the fuel ports.

The assessment of the degree of stratification was carried out in non-reacting flows with planar laser-induced fluorescence (PLIF) of acetone seeded into the "fuel" stream. The instantaneous PLIF images revealed the distribution of equivalence ratio in the flow field. It was noted that the fuel-rich pockets are frequent near the outer wall, but there is an intermittent presence of these pockets near the center-body. In the mean sense, the flow near the outer wall is richer ($\phi \sim 1.0$-1.5 for methane, $\phi \sim 0.5 - 0.6$ for hydrogen) than near the center-body. These equivalence ratios correspond to unstretched laminar flame speeds as high as 0.30 m/s and 1.5 m/s for methane and hydrogen, respectively. In an instantaneous sense, the maximum equivalence ratios were higher for both methane and hydrogen, which corresponded to maximum unstretched laminar flame speeds of 0.30 m/s and 3.0 m/s. Thus, in an instantaneous sense, hydrogen-air has faster propagation speed by an order of magnitude.

Simultaneous high-speed luminosity imaging and stereoscopic PIV measurements were captured at 4 kHz. In the intermediate stabilization mode, it was observed that there are bright flame structures near the leading edge of the flame, which grow in time until they merge with the flame brush. These flame structures seem to follow the path of the swirling flow, which indicates that the effect of flame tongue's blockage is not a dominant factor in flame-flow interaction. Instead, it is noted that the bright flame structures impose strong blockage on the approach flow. However this blockage is not sustained in time, thus any assistance in upstream propagation of flame is not there. The case of hydrogen-rich flame is different though.

The flame profile captured in the laser sheet plane confirmed the presence of flame structure on the outer wall during hydrogen-rich flashback. The simultaneous luminosity imaging revealed the presence of acute-tipped flame structures on the outer wall. The outer wall propagation of the flame occurred in two distinct phases. In the first phase, the formation of the acute-tipped flame structure initiates upon interaction of bright flame structures with the outer wall. In this phase, the flame structure resists the approach flow without making much movement in the axial or azimuthal direction. The next phase is marked with the flame advancement towards the fuel ports. In this phase, the flame tip catches on to near stoichiometric mixtures along the outer wall. The flame structure gets brighter as it approaches the fuel ports.

The elevated pressure experiments revealed the role of turbulence in breaking the fuel-parcels into smaller fuel rich pockets. These fuel rich pockets appear as bright flame structures at the leading edge of the flame tongue, however the sizes of bright flame structure are millimeter scale. This flame structure does not affect the flow as much as atmospheric pressure counterpart. For elevated-pressure hydrogen-rich flashback, the mechanism of acute flame anchoring was the same as that of atmospheric pressure flashback. However, at the flame advancement stage, the flame propagated as a wide flame brush along the outer wall.

C. Publications Resulting from this Project

[1] Tang, Y., Hassanaly, M., and Raman, V., "Numerical Study of Flame Stabilization Mechanism in a Premixed Burner with LES Non-adiabatic Flamelet Approach." APS Division of Fluid Dynamics Meeting Abstracts. 2015.

[2] Tang, Y., Koo, H., Leitz, C., and Raman, V., "Numerical Study on Flame Stabilization Mechanism of a multi-jet burner with LES Flamelet Approach." 54th AIAA Aerospace Sciences Meeting. 2016.

[3] Tang, Y., Hassanaly, M., and Raman, V., "Numerical Simulation on Lean Premixed High Swirl Flame Flashback." SIAM 16th International Conference on Numerical Combustion. 2017.

[4] Tang, Y., Hassanaly, M., and Raman, V., "Numerical study of swirl boundary layer flashback using LES-based tabulation method based on premixed and diffusion flamelet." Bulletin of the American Physical Society. 2018.

[5] Ranjan, R., Ebi, D. and Clemens, N.T., "Role of inertial forces in flame-flow interaction during premixed swirl flame flashback," *Proceedings of the Combustion Institute*, to be published 2019.

[6] Ebi, D., Ranjan, R. and Clemens, N.T., "Coupling between premixed flame propagation and swirl flow during boundary layer flashback," Experiments in Fluids, Vol. 59, Issue 7, p. 109, 2018.

[7] Ranjan, R. and Clemens, N.T., "High-repetition rate stereoscopic PIV investigation of stratified swirl flame flashback at atmospheric and elevated pressures," 18th International Symposium on Applications of Laser and Imaging Techniques to Fluid Mechanics, Lisbon, July 2016.

[8] Ranjan, R. and Clemens, N.T., "Time-Resolved Three-Component PIV Investigation of Flashback in Stratified Flames," ASME TurboExpo, June 2017.

[9] Ranjan, R., Ebi, D. and Clemens, N.T., "Time-resolved stereoscopic PIV measurements of boundary layer flashback in premixed flames at elevated pressures," 11th International Symposium on Particle Image Velocimetry, Santa Barbara, California, September 2015.

D. ACRONYMS

2D	two dimensional
3D	three dimensional
BPR	back pressure regulator
BV	ball valve
CCD	charge coupled device
CMOS	complementary metal oxide semi-conductor
CV	control valve
FGM	flamelet generated manifold
FLOX	flameless oxidation
FPVA	flamelet/progress variable approach
FWHM	full width at half maximum
JICF	jet in crossflow
LES	large-eddy simulation
l.h.s.	left hand side
MFC	mass flow controller
N.A.	not applicable
Nd:YLF	Neodymium: Yttrium Lithium Fluoride
PIV	particle image velocimetry
PLIF	planar laser-induced fluorescence
r.h.s.	right hand side
SNR	signal-to-noise ratio
SV	solenoid valve
UT	University of Texas
UV	ultraviolet